Expertise
and insight
for the future

Evgeny Slivinskiy

Wireless Optical Link Design and Fog Loss Measurements

Metropolia University of Applied Sciences

Bachelor of Engineering

Electrical and Automation Engineering

Bachelor's Thesis

20 April 2019

Author(s)	Evgeny Slivinskiy
Title	Wireless Optical Link Design and Fog Loss Measurements
Number of Pages	37 pages + 4 appendices
Date	20 April 2019
Degree	Bachelor of Engineering
Degree Programme	Electrical and Automation Engineering
Professional Major	Automation Engineering
Instructor(s)	Timo Tuominen, Senior Lecturer Markku Vainio, Project Manager

Deployment of 5th generation of mobile networks leads to an increasing demand for high-speed access interfaces. The challenge of finding an alternative to fiber optics used now as a link between the centralized radio controllers and the radio heads can be overcome by implementation of wireless optical communication technology. However, despite of many advantages of this technology, weather conditions impede its reliable operation. Being relatively immune to rain and snow, traditional wireless optical systems of near-infrared wavelengths suffer from atmospheric turbulence and especially fog.

To explain interruptions of operation of wireless optical links in fog, an experimental setup consisting of a mid-infrared (9.2 µm) quantum cascade laser (QCL) link, a near-infrared (1.55 µm) laser link, and a visible (0.532µm) laser link was built during the project.

Droplet size distributions at different fog stages were deducted from direct extinction of multi-wavelength signals. This allows to better understand fogs dynamics and their influence on link losses that can help to develop more reliable solutions of wireless optical technology.

Comparison of standard telecom diode laser and mid-infrared QCL beams loss in dense fog conditions proved that QCL could be considered as an effective source of signal for wireless optical links.

Keywords	wireless optical link, free space optical communication, quantum cascade laser, scattering loss

Tekijä Otsikko Sivumäärä Aika	Evgeny Slivinskiy Langattoman optisen linkin suunnittelu ja sumusta riippuvien optisten häviöiden kartoittaminen 37 sivua + 4 liitettä 21.4.2019
Tutkinto	insinööri (AMK)
Tutkinto-ohjelma	sähkö- ja automaatiotekniikkaa
Ammatillinen pääaine	automaatiotekniikkaa
Ohjaajat	vanhempi lehtori Timo Tuominen projektijohtaja Markku Vainio

5G-tietoliikenneverkkojen käyttöönoton myötä tukiasemien ja runkoverkon väliseltä liityntäverkolta vaaditaan yhä nopeampia tiedonsiirtonopeuksia. Nämä yhteydet on perinteisesti toteutettu kuituoptisin linkein, joille kuitenkin etsitään vaihtoehtoja mm. kustannustehokkuuden parantamiseksi. Eräs mahdollinen vaihtoehtoinen ratkaisu on langaton optinen tiedonsiirto, jonka siirtotien luotettavuus kuitenkin kärsii sään aiheuttamista häiriöstä. Perinteinen, lähi-infrapuna-alueen aallonpituuksia hyödyntävä langaton optinen tiedonsiirto on suhteellisen immuuni vesi- ja lumisateelle, mutta häiriintyy ilmakehän turbulenssista ja erityisesti sumusta.

Tässä hankkeessa tutkittiin langattomien optisten linkkien toimintaa erilaisissa sumuolosuhteissa käyttäen kolmea eri aallonpituudella toimivaa vapaan tilan laserlinkkiä, jotka suunniteltiin ja rakennettiin hankkeen aikana: Uuteen kvanttikaskadilaserteknologiaan perustuva keski-infrapuna-alueen (9,2 µm) linkki, optisen tietoliikenteen lähi-infrapuna-alueella (1,55 µm) toimiva linkki, sekä näkyvän aallonpituuden (0,532 µm) linkki. Näiden linkkien optisten signaalien vaimentumista tutkittiin erilaisissa sääolosuhteissa niin laboratorio- kuin kenttäkokein.

Kolmella aallonpituusalueella samanaikaisesti tehtyjen vaimennusmittausten avulla voitiin selvittää sumupisaroiden kokojakaumat eri sumutyypeissä sekä sumunmuodostumisen eri vaiheissa. Näin kerätty tieto auttaa ymmärtämään sumun muodostumisen ja hälvenemisen dynamiikkaa, sekä sumun vaikutuksia optisten signaalien vaimenemiseen. Tämä puolestaan auttaa entistä luotettavampien langattomien optisten tiedonsiirtolinkkien toteuttamisessa.

Hankkeen aikana tehdyt vertailut perinteisen optisen tietoliikennealueen ja keski-infrapuna-alueella toimivan kvanttikaskadilaserteknologian välillä osoittivat, että kvanttikaskadilaserit ovat lupaava vaihtoehto tulevaisuuden langattomaan optiseen tiedonsiirtoon

Avainsanat	langaton optinen linkki, optinen tiedonsiirto vapaassa tilassa, kvanttikaskadilaser, sirontahäviö

Contents

List of Abbreviations

BBU	Base Band Unit
BSC	Base Station Controller
BTS	Base Stations Transceivers
CPRI	Common Public Radio Interface
C-RAN	Cloud RAN
DSD	Droplet Size Distribution
EMI	Electromagnetic Interference
FSO	Free Space Optical communications
ITU	International Communication Union
LiDAR	Light Detection and Ranging
LOS	Line of Sight
LTE	Long Term Evolution
MIMO	Multiple Input Multiple Output
MIR	Middle Infrared Range
mmW	Millimeter-Wave technology
MQTT	Message Queuing Telemetry Transport protocol
NLOS	Non-Line of Sight
NIR	Near Infrared Range
PMT	Point to Multipoint
PoE	Power over Ethernet
PTP	Point to Point
QC	Quantum Cascade
QCL	Quantum Cascade Laser
RAN	Radio Access Network
RF	Radio Frequency
RRH	Remote Radio Head
RRU	Remote Radio Unit
SNR	Signal Noise Ratio
TEC	Thermo Electric Cooler
WDM	Wavelength Division Multiplexing
WOC	Wireless Optical Communications
X2	LTE interface between Evolved Node Base Stations

1 Introduction

1.1 5G Networks Challenges

The 5th Generation (5G) is the next generation of Mobile Communication Networks, which will integrate 4th Generation (4G) or Long-Term Evolution (LTE) mobile networks.

According to an International Communication Union (ITU) document [1], 5G networks should have a peak data rate of 20 Gb/s for the downlink and 10 Gb/s for the uplink. Latency is declared as four milliseconds in a mobile scenario, and as one millisecond in Ultra Reliable Low Latency Communication scenarios. The network should provide connections between people, machines, automobiles, city infrastructure, public safety etc.

Deployment of the 5G networks leads to an increasing demand for high capacity, low latency, high availability and high-speed access interfaces. A comparison of 5G network requirements with the current state of existing 4G networks is presented in Figure1.

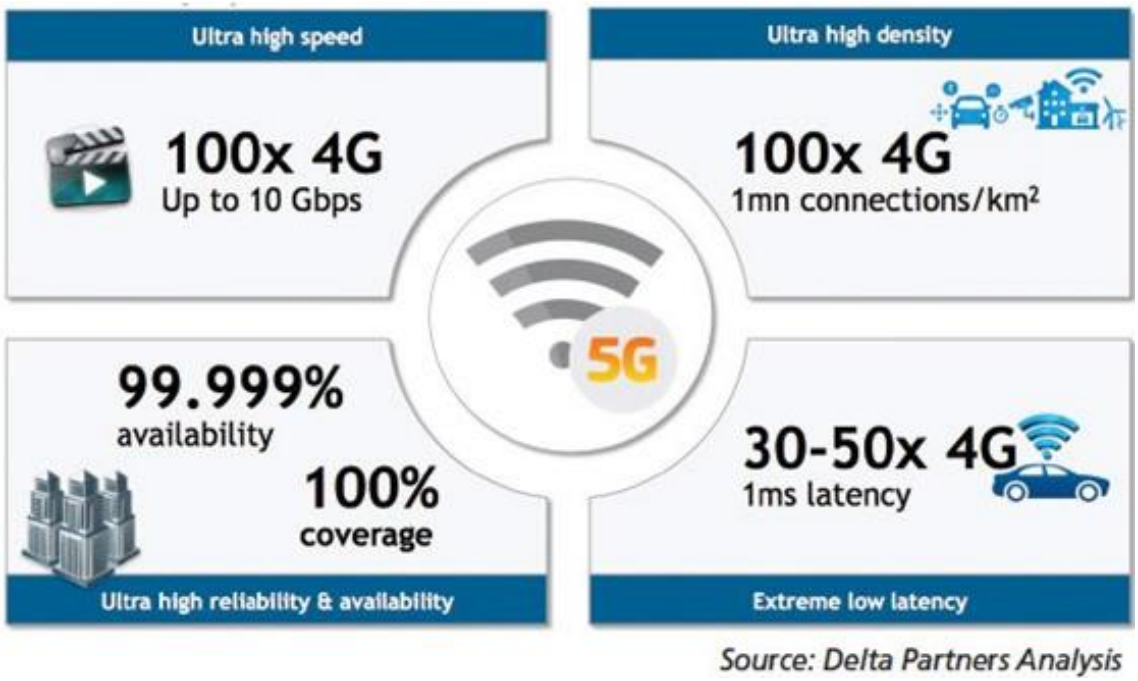

Figure 1. 5G key requirements, picture from [2].

1.1.1 C-RAN Architecture

All above mentioned specifications are not possible without the new concept of network architecture known as the Centralized/Cloud Radio Access Network (C-RAN). To meet availability and coverage demands, 5G network cell density must be increased. If for 3G networks the amount of base stations is 4-5 per km², for 4G networks 8-10 per km², estimations for 5G networks reach 40-50 base stations per km². Then, each base station could provide transport links up to 25 Gbit/s, with up to 100 Gbit/s backhaul links [3].

From traditional Base Stations Transceivers (BTS) with Baseband and Transport functions located at each cell tower and connected to the antennae by coaxial cabling (see Figure 2) mobile networks operators are migrating to small cells (Appendix 1, Figure 1), distributed antenna systems and C-RAN (see Figure 3).

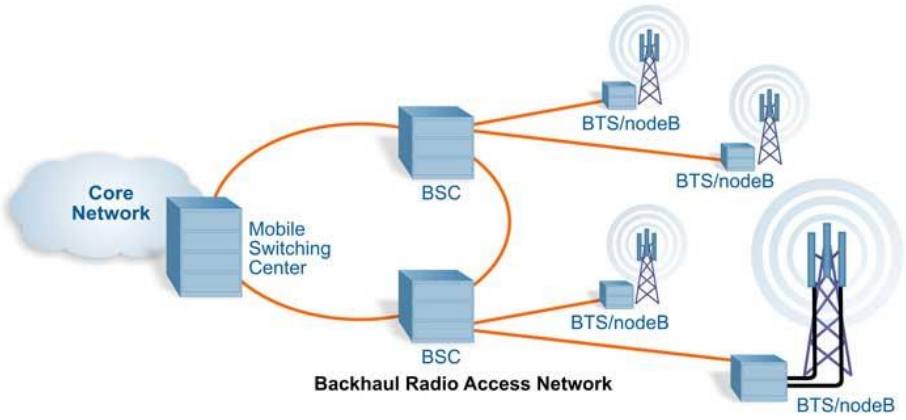

Figure 2. The traditional 3G network architecture from [4]. Optical fiber is drawn by orange, coaxial cable is black.

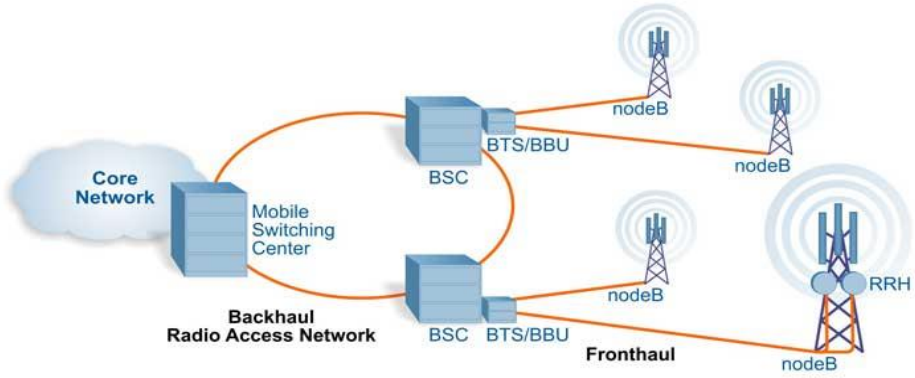

Figure 3. Cloud-based Radio Access Networks 4G architecture from [4]. Optical fiber is drawn by orange.

C-RAN contains three main components - Base Band Unit (BBU), fronthaul network, and Remote Radio Head (RRH). The BBU combined with a Base Station Controller (BSC) converts the network data to a signal that can be used to modulate the carrier frequency for transmission, while compact RRH, located close to an antenna tower contains radio frequency equipment. The BBU is connected to the RRH by fiber using digital radio over fiber protocol such as Common Public Radio Interface (CPRI) [4]. Links between RRHs and the Core Network are divided into Fronthaul and Backhaul transport channels.

More detailed review of RAN evolution can be found in Appendix 1(Figure 2).

1.1.2 5G Fronthaul Requirements

One of the most serious challenges facing 5G network designers is ultra-high radio speed which leads to enormous traffic at fronthaul (see Figure 4).

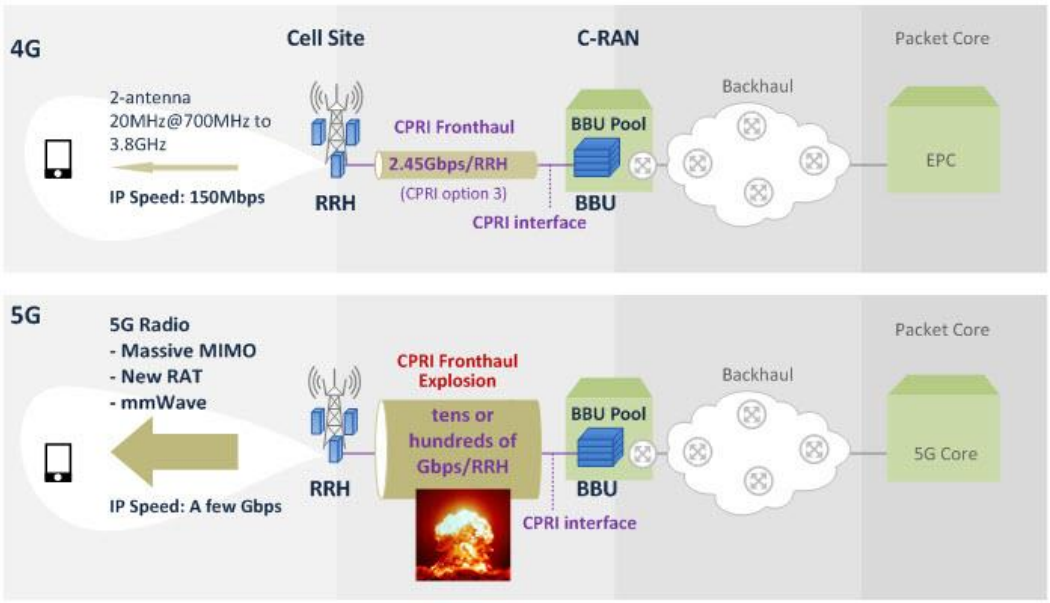

Figure 4. Common Public Radio Interface fronthaul explosion due to ultra-high radio speed [5].

While LTE networks have for the C-RAN/Fronthaul the maximum transmission capacity per CPRI port 10Gbps (starting at 2.5 Gbps and may growing to more than 10 Gbps in the coming years) 5G Fronthaul capacity must be enhanced drastically (minimum requirement is 25Gbps) [5]. The most suitable solution in stationary case is an optical fiber with Wavelength Division Multiplexing (WDM). But installation of fiber cables requires permissions, expensive digging, time consuming, and in some cases is not possible at all.

RF wireless solutions, for example millimeter-wave (mmW) technology, are in some cases an alternative to fiber optic technology. Millimeter-wave link frequencies such as 28-38 GHz, and 60 GHz, as well as the E-band (70-90 GHz) are the alternatives in wireless backhaul infrastructure to enable 5G networks. The E-band provides higher spectral resource compared to traditional microwave bands (6–42 GHz). However, the high capacity of E-band mmW links require line-of-sight, and the link distance is short due to an oxygen absorption and strong signal attenuation by rain. Current 60GHz systems, in fact, are limited in a range to about 1 km due to oxygen absorption in the atmosphere, even without rain.

Moreover, RF networks with very dense multiple antennas suffer from electromagnetic interferences and lack of available radiofrequency spectrum. The fact that many RF bands are licensed can significantly raise costs and even bar operators from entry. Licensing, however, is a necessary, because it mitigates another one of RF's challenges – interference. For successful development of 5G mobile networks it is important to find a solution which could replace the fiber optics now used to implement the BBU-RRH links and limited capacity mmWaves systems. One of the potential options might be wireless Free-Space Optical technologies [6].

1.2 Free Space Optical Communications

Free Space Optical (FSO) communications relates to several wireless optical data transmitting technologies that use air or vacuum for line-of-site light propagation.

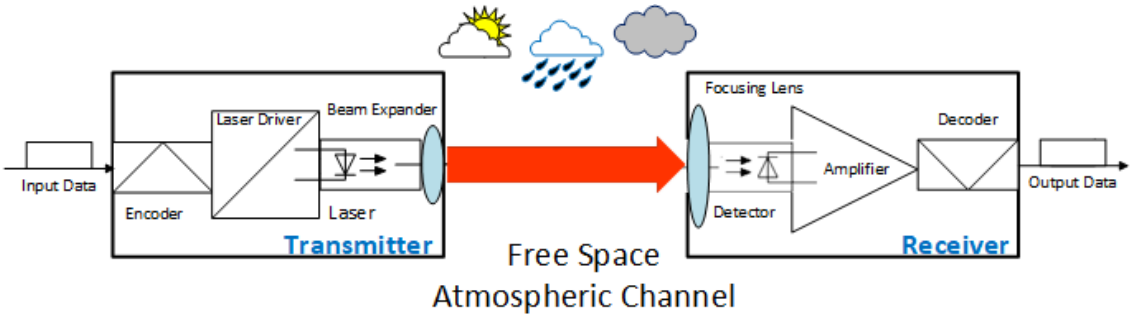

Figure 5. Basic FSO communication link.

Basic FSO link (see Figure 5) transmits optical signal in one direction – from transmitter to receiver separated by certain distance. The digital input data which has to be transmitted are modulated by encoder on the amplitude, frequency or phase of the carrier light. High-power

semiconductor laser with customized power supply (Laser Driver) serves as a source of modulated light beam. The beam forming optical system (Beam Expander) transforms diverging laser beam so that the optical signal on the receiver side would have detectable power density. Focusing lens of the receiver concentrates input signal on the high sensitivity photon detector, and the amplifier converts low signal level into the suitable for the decoding values.

Design of main parts of the basic FSO link made on a base of Quantum Cascade (QC) laser will be more detailly described in the following sections of the Chapter 2:

- Beam Forming Optics (2.1) – calculations of parameters of beam expander of the transmitter and focusing lens of the receiver,
- Mechanics of the Transmitter (2.2.1) and the Receiver (2.3.1) – functions of elements of the opto-mechanics,
- Electronics of the Transmitter (2.2.2) and the Receiver (2.3.2) – electrical scheme and components description.

Traditionally, wavelengths of light of semiconductor lasers within atmospheric transparency windows (see Figure 6) in the ranges 780-850 nm and 1520-1600 nm are used for FSO. A modulated beam of the laser light is a carrier of transmitted signal, and the frequency of the light is considered as the carrier frequency.

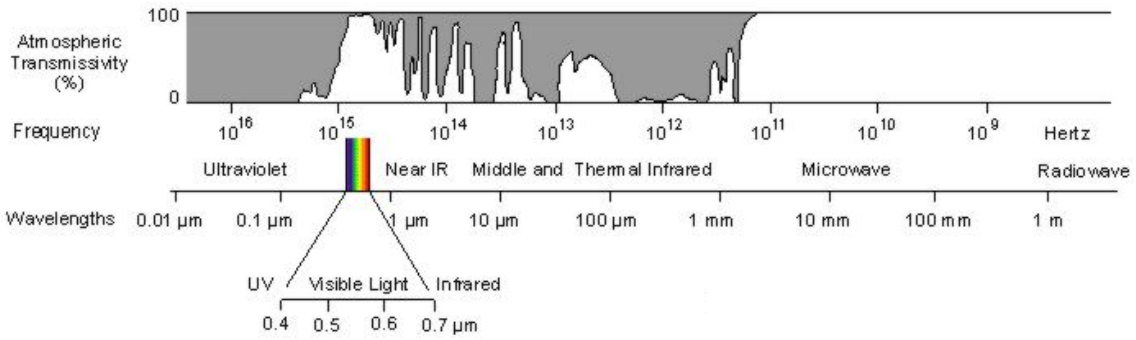

Figure 6. Atmospheric transmission windows frequencies and wavelengths. Picture from [7].

For example, wavelength of 1.5 µm corresponds to 199 861 GHz, and a 100 GHz channel bandwidth (difference between the upper and lower frequencies in a continuous band of frequencies) corresponds to less than 1 nm of wavelength spread while for the most advanced 3.3 mm wave carrier frequency corresponds to 90 GHz.

1.2.1 FSO -Current Situation

Owing to its high potential capacity, relatively simple beam forming, immunity to electromagnetic interferences, relatively low cost and rapid deployment (no digging), FSO communication links could be a promising alternative in transferring data at high rates over short (up to one kilometer) distances.

The development of FSO technologies was actively supported by the US and NASA military in the nineties and was used in various forms for communication. Starting from 1998, substantially more than one billion dollars have been spent for R&D of terrestrial FSO by different governmental and private investors [8]. During this time, new light sources such as QC lasers and laser beam auto aiming systems have become affordable. Commercially available FSO equipment specifies full duplex communication up to 30 Gbit/s for 1.3 km and 1 Gbit/s up to 15 km [9]. But despite of all above mentioned, the use of FSO systems as a part of telecommunication network infrastructure is very limited. The main reason for this is the modest up-time that can be guaranteed with the existing FSO link technology. Depending on geographical location and weather conditions, the maximum up-time of the commercially available FSO links is often limited to 95-97% at link spans longer than 200 m. A practical way for the most FSO equipment manufacturers to achieve 5G network standard requirement of more than 99.99% up-time is by including an additional RF link. It operates with decreased capacity in case of the optical link goes down.

1.2.2 FSO Limiting Factors

The limitations of atmospheric channel are the main problems for reliable FSO system implementation. Flying objects like birds, insects and tree leaves can interrupt narrow optical beam for a short time. Wind, temperature jumps, and building sway can result in misalignment of a beam positioning system. Atmospheric turbulences or scintillations may affect the propagating beam shape and pointing due to index of refraction fluctuations, and these distortions decrease a signal noise ratio of modulated light. But the most critical attenuation of transmitting optical signal caused by precipitations. Among hydrometeors (rain, snow, hail) a fog gives the strongest attenuation of optical beam. The most commonly used traditional FSO systems based on semiconductor lasers at wavelengths 0.85 µm and 1.55µm are very sensitive to even small

concentrations of 0.1-10 µm water droplets due to Mie scattering and cannot provide the demanded 99.99% availability even in a moderate fog. [10;11;12]

2 99.99% FSO Communication Project

The advent of 5G networks brings a new market for FSO systems and has led to search of new technical solutions to improve the reliability and up-time of wireless optical links. In the plan of University of Helsinki project "99.99% Free Space Optics Communication" supported by Business Finland founding agency, the use of mid-infrared quantum cascade lasers (QCLs) was proposed as a potential solution to reduce FSO link scattering losses due to fog.

2.1 Project Prerequisites

Various QCL types over the 4-11 µm mid-infrared (MIR) wavelength range with output powers of up to 1W became affordable recently. The wavelength range around 10 µm (7-11µm) looks attractive for optical communication due to high atmosphere transparency, low solar radiation, low refractive index of air, low scattering efficiency, and eye safety. The reason why the MIR optical communications still have not been used is simple: FSO at this region is an emerging technology.

The foremost feature of QCL which makes it suitable for telecommunication is its ability to high frequency modulation. Theoretically computed on a base of photons lifetime the frequency response of -3dB at twice threshold current is about 11 GHz for QCL structures, with ultrafast modulation capability up to 100 GHz. Estimation of RC time constant of electrical response in an absence of all parasitic components gives 7ps that corresponds to frequency of 21 GHz. [13]

That suggest of all-optical modulation approach advantage at design of ultra-fast FSO link. Experimental demonstration of standard QCL MIR optical emission amplitude modulation up to 10.35 GHz at cryogenic temperatures has been made in the work [14], optically induced high-speed frequency modulation and wavelength modulation schemes are described in [15;16].

Possible implementation of all-optical modulation at ambient temperature for MIR QC lasers could solve the problem of extremely high (25-100 Gbps) requirements to capacity of fronthaul and midhaul of 5G mobile communication networks (see Figure 7).

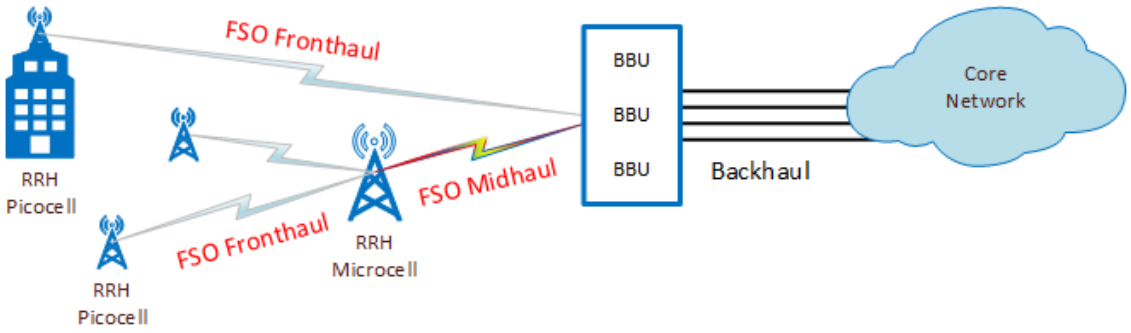

Figure 7. Potential application of FSO link in 5G network data transport solutions.

2.2 Project Plan Implementation

The project plan included building of a prototype of QCL based FSO link consisting of transmitter and receiver, experimental comparison of attenuation of 1.55 µm (standard telecom diode laser) and 9.22 µm QCL beams in a laboratory ultrasound artificial fog as well as in real outdoor conditions of natural fogs. The project plan chart is presented below in the Figure 8.

The project was started from extensive literature search and model calculations (described in Section 3.1) to determinate the technical requirement for prototype design. At the end of the first stage, when demands to specifications of transmitter and receiver became in accordance to planned distances and output signal intensities, the parts purchasing process was initiated.

The second stage of the project included 3D design of opto-mechanical - involving both optical and mechanical elements - construction (described in Sections 3.2.1 and 3.3.1), a search of solutions for transmitter and receiver electronics (described in Sections 3.2.2 and 3.3.2), a choice of data acquisition system (described in Chapter 4.1 and 4.2). 3D design allowed to avoid mistakes and to find suitable solutions using 3D drawings of commercially available parts from catalogs of optics and mechanics suppliers. Ready-made enclosures were transformed to experimental stand that gave us possibility to change displacement of our mounts and estimate serviceableness for potential production. Standard mechanics and electronics components helped to accelerate the

prototype implementation. Experiment-oriented data acquisition system made possible both a laboratory and on-field tests.

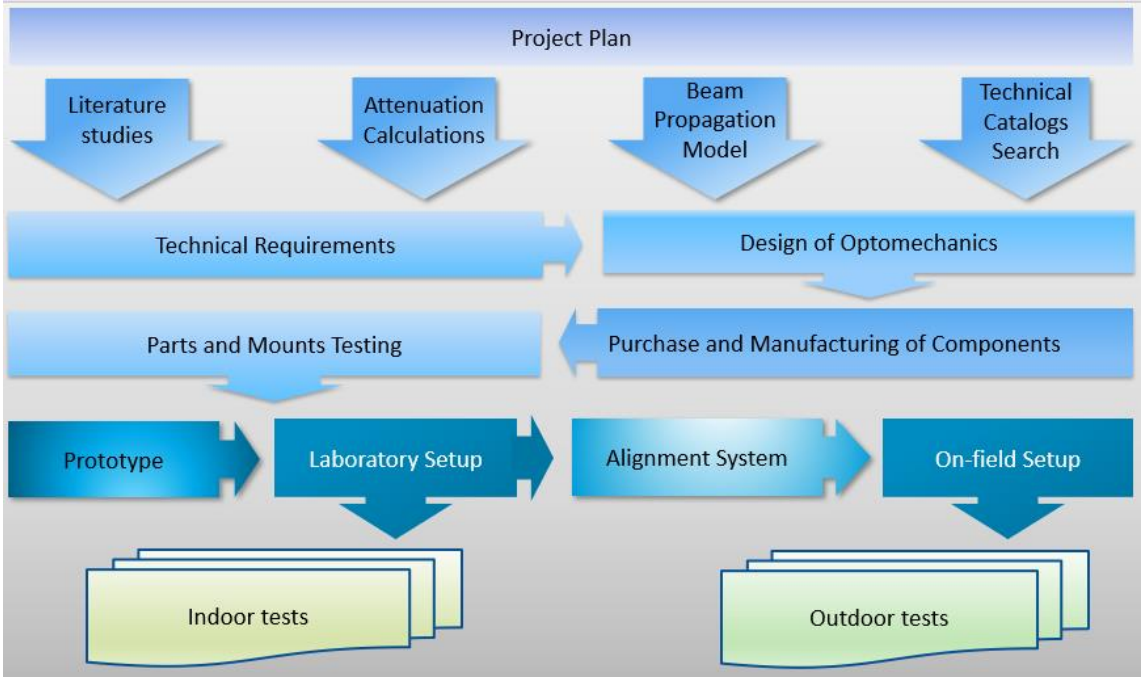

Figure 8. 99.99% Free Space Optics Communication project plan.

At the third stage, after completion of the prototype assembly, a series of laboratory experiments with simulating conditions of continental and marine fogs were carried out (described in Section 5.1). The data were analyzed, and measured attenuations were calculated to common used attenuation on meteorological visibility dependencies that allows to compare our results with results of other experimental groups. Additionally, the droplet size distributions generated in the tests were reversely deducted from specific extinction ratios of different wavelength light beams.

Before on-field experiments a beam position alignment system with manual adjustment suitable was designed for distances up to 40 m. Then the link prototype was installed on a building roof for testing and signal attenuation measurements in real all-weather conditions (described in Section 5.2).

After a series of summer-autumn tests the alignment system and enclosures of the transmitters/receivers were improved for winter conditions. The beam alignment was motorized,

equipped with Bluetooth driven remote control of the motors, and the enclosure was enforced against wind gusts. These improvements made the link suitable for distances of more than 60 m.

Rigorous multi-wavelength characterization of the attenuation of free-space optical links in various fog conditions has been done during the project. This work helps to better understand fog dynamics and their influence on FSO link losses. This research paves the way for FSO communication links for applications like 5G fronthaul and backhauls, where high link reliability (>99.99% up-time) is necessary.

3 Prototype Design

The prototype of wireless optical link is intended for experiments that are designed to test the advantages and disadvantages of QC lasers in FSO applications, to conduct link attenuation tests, as well as to further optimize the link design and components. The requirements to prototype design are presented in Figure 9.

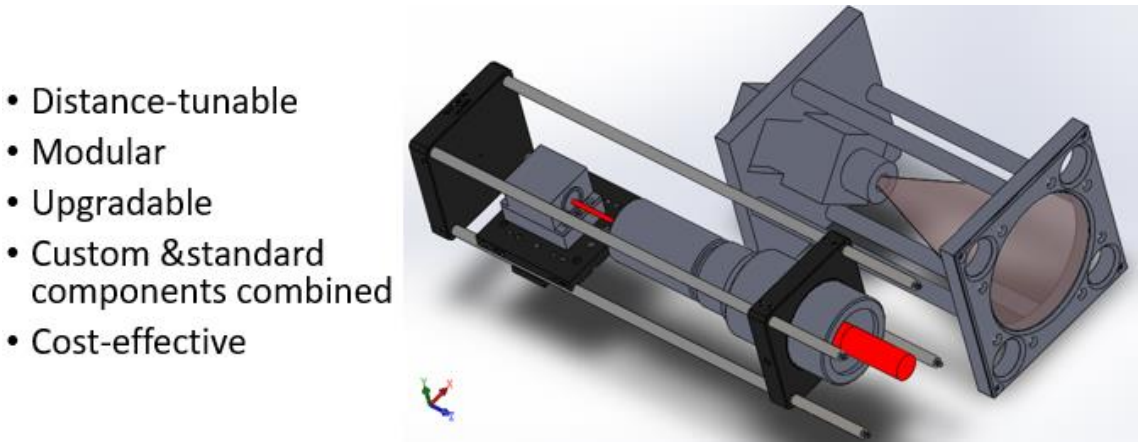

Figure 9. The project requirements to the prototype design.

The design of the prototype includes solutions related to optics, fine-mechanics, laser driver electronics, fine mechanics of alignment system, weather protections etc. Even the first version of the link must provide a stable operation of the equipment at continuous all-weather test conditions. Prototype design solutions should provide tunability in 30-200 m distance range, be flexible for potential parts replacement and transportation from one place to another.

Despite of experiment-oriented design of the prototype, certain solutions can be applied at commercial version of the link hence utilizing of tested standard parts and components simplifies

engineering of final product. Moreover, for mass production, it is essential to find cost-effective solutions, reliable suppliers, and short logistics chains already at the stage of prototype design. Real conditions of on-field tests impose certain restrictions on the design. For example, testing on a roof involves compliance to electrical safety rules, that means using of PoE power supplies and leads to strict power consumption limits.

In Figure 10 is shown a photograph of the MIR link prototypes developed in this thesis work. The prototype consists of a transmitter unit (left) and a receiver unit (right).

Figure 10. External view of the prototype of MIR link.

3.1 Beam Forming Optics

The beam forming optical system consists of a beam expander of the transmitter and a focusing lens of the receiver. A collimating lens of the semiconductor laser forms a beam with a certain diameter, divergence and quality factor. This beam must have the proper diameter and shape suitable to keep a tolerance to misalignment at temperature drifts, wind, vibrations, and to provide detectable power density at harsh weather conditions like rain, haze, and fog. The receiver lens must have as big as possible size to eliminate spatial inhomogeneities of the beam passed through the atmospheric channel. Additionally, using of a narrow band spectral filter is needed for separation of optical signal from parasitic radiation of the Sun or other radiating objects.

3.1.1 Beam Size Calculation

During the design of the optical scheme, the most important parameter to be taken in account is the laser beam size on a distance required. The choice of optical as well as electronical

components of the prototype construction depends on light power density at the detector input window.

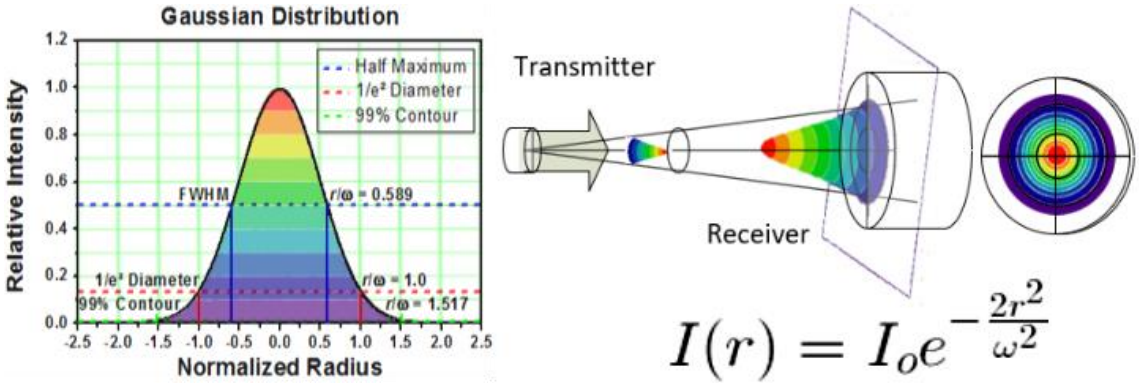

Figure 11. Gaussian beam characteristics, modified picture from [17].

The QC laser selected for the project (specified in Section 3.2.2) has an output beam with a Gaussian distribution of intensity that needs to be taking in account at input signal power density calculations. Left part of Figure 11 describes parameters of Gaussian intensity distribution in the radial direction, orthogonal to the direction of the light propagation in a plane of receiver, as it is illustrated in right part of the picture.

The QCL maximum output light power of 75 mW at 25ºC for long-term reliable operation must be lowered to 80%, or not more than 60 mW will be considered as output power. Even at optimal alignment, optical channel loss could be up to 60% due to IR optics loss, and probably misalignment adds up to 20% of loss. So, the Gaussian beam power distributed over the receiver window is estimated to be 20-25 mW.

The photoelectromagnetic light detection unit (specified in Section 3.3.2) has voltage responsivity 23 V/W, and the data acquisition system input voltage should be not less than 100 mV for reasonable signal dynamics.

Based on above mentioned assumptions and values, well aligned optical link with standard receiver input lens of 50 mm (2 inch) in diameter could provide for the acquisition system up to 300 mV when the laser beam diameter is about 150 mm at the receiver (see Figure 12). This diameter value seems to be a good compromise between the level of output signal and tolerance to misalignment, atmospheric fluctuations and mechanical vibrations.

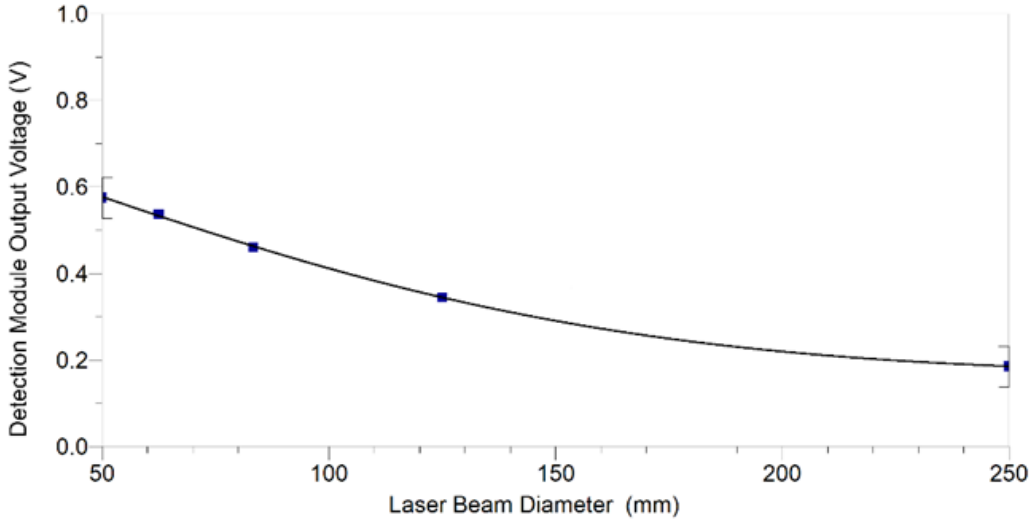

Figure 12. Dependence of output voltage of the detection module on the laser beam size.

3.1.2 Beam Expander Magnification

A free space propagating beam of laser light of initial diameter *d* increases with a distance *L* to diameter *D*. Divergence θ is an angular value of the increase (see Figure 13).

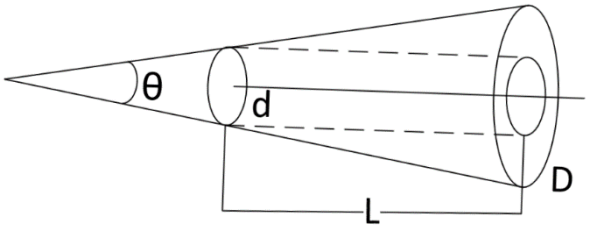

Figure 13.Optical divergence illustration.

In simplified case, beam diameter *D* on distance *L* can be calculated with a simple Formula 1:

$$D = d + L \times tan\theta \qquad (1).$$

The initial diameter *d* and divergence θ of the QC laser given in specifications are about 3 mm and 2 mrad (2.04 mrad in lateral plane, 1.6 mrad in vertical plane) respectively, that means for unmagnified beam about 4m beam diameter on the distance of 200 m (see Figure 14, Magnification power=1). If the diameter of a beam increases by thousand times, its area will be increased by million times, hence beam power density will be decreased by million times.

To get sufficient beam power density on a long distance, the divergence must be decreased. Since a beam expander will increase an input beam diameter by magnification *M=D/d* and decrease an input divergence by it as well, received beam size is expressed by Formula 2:

$$D = M \times d + L \times tan\frac{\theta}{M} \quad (2).$$

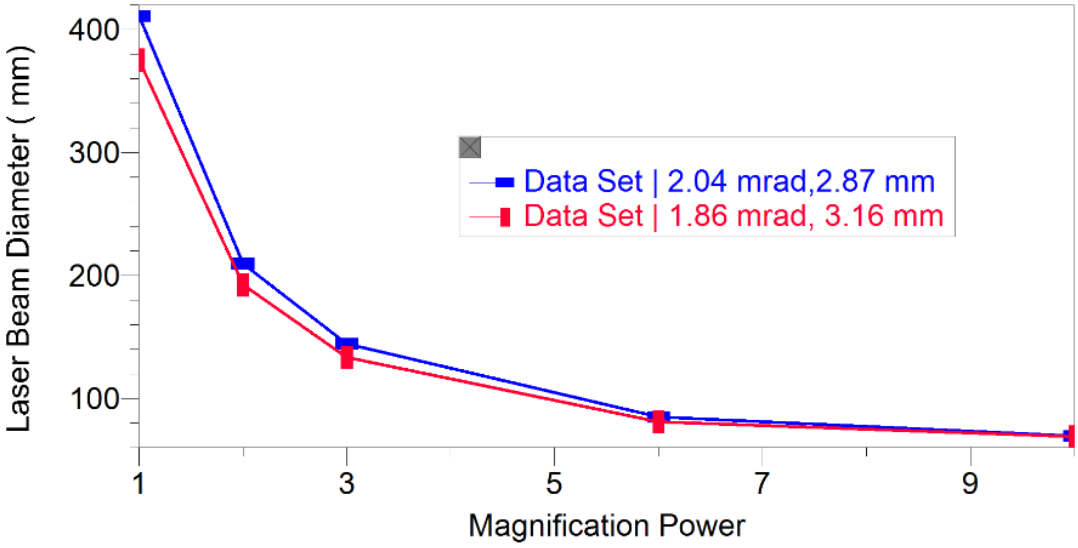

Figure 14. Beam on diameter the distance of 200 m calculated in accordance with Formula 2.

Unfortunately, such a coarse approach in the case of real laser beam with different divergence at lateral and vertical optical planes gives significant error in beam size calculation on distances of tens of meters. A more advanced solution for this problem was obtained using a MathCad model of the QCL beam propagation based on the ray transfer matrix analysis or ABCD ray matrices method described in [18;19].

Laser dependent parameters of the model (see Figure 17 below):

- wavelength – λ,
- beam radius (Lateral, $1/e^2$) at specified waist distance Z_{0L} – W_{0L},
- beam radius (Vertical, $1/e^2$) at specified waist distance Z_{0V} – W_{0V},
- quality factor – M^2 [20].

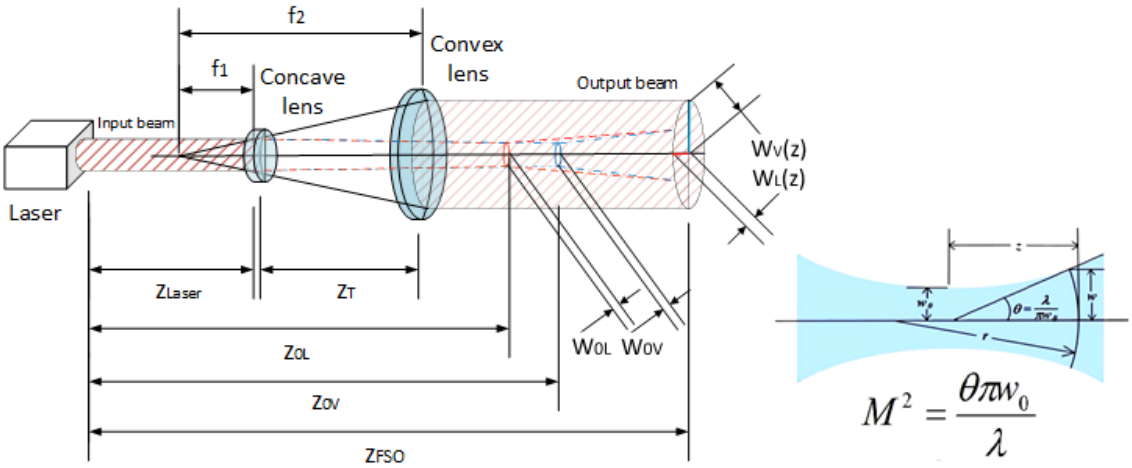

Figure 15. Parameters are used in the ray matrices model. Quality factor M2 drawing from [20].

Beam forming optical scheme parameters of the model:

- focal length of the 1st lens – f_1,
- focal length of the 2st lens – f_2,
- distance of the 1st lens from laser – Z_{Laser},
- distance between the lens – Z_T,
- distance to the target – Z_{FSO}.

In the model an optical propagating beam is considered as a slow diverging wave. This wave interacts with elements of optical system which are described by proper matrices. For example, propagation in free space media is described by $\begin{pmatrix} 1 & d \\ 0 & 1 \end{pmatrix}$ matrix, where d is a distance, and thin converging convex lens $\begin{pmatrix} 1 & 0 \\ -\frac{1}{f} & 1 \end{pmatrix}$, where f is focal length of lens.

After combination of different matrices, the beam propagation matrixes for free space propagation over distance Z_{FSO} after the telescope are presented below:

$$M_{TL}(Z_{FSO}) = \begin{pmatrix} 1 & z_{FSO} \\ 0 & 1 \end{pmatrix} \begin{pmatrix} 1 & 0 \\ -\frac{1}{f_1} & 1 \end{pmatrix} \begin{pmatrix} 1 & z_T 0 \\ 0 & 1 \end{pmatrix} \begin{pmatrix} 1 & (z_{Laser} - z_{0L}) \\ -\frac{1}{f_2} & 1 \end{pmatrix} \quad (3),$$

$$M_{TV}(Z_{FSO}) = \begin{pmatrix} 1 & z_{FSO} \\ 0 & 1 \end{pmatrix} \begin{pmatrix} 1 & 0 \\ -\frac{1}{f_1} & 1 \end{pmatrix} \begin{pmatrix} 1 & z_T 0 \\ 0 & 1 \end{pmatrix} \begin{pmatrix} 1 & (z_{Laser} - z_{0V}) \\ -\frac{1}{f_2} & 1 \end{pmatrix} \quad (4).$$

Taking in account the quality parameters:

$$q_{TL}(z_{FSO}) = \left(\frac{M_{TL}(z_{FSO})_{0,0}\cdot q_{0L}+M_{TL}(z_{FSO})_{0,1}}{M_{TL}(z_{FSO})_{1,0}\cdot q_{0L}+M_{TL}(z_{FSO})_{1,1}}\right) \quad (5),$$

$$q_{TV}(z_{FSO}) = \left(\frac{M_{TV}(z_{FSO})_{0,0}\cdot q_{0V}+M_{TV}(z_{FSO})_{0,1}}{M_{TV}(z_{FSO})_{1,0}\cdot q_{0V}+M_{TV}(z_{FSO})_{1,1}}\right) \quad (6).$$

Then the beam radii can be calculated from the q-parameters as follows:

$$w_{L\_tele}(z_{FSO}) = \sqrt{\frac{\lambda}{-Im\left(\frac{1}{q_{TL}(z_{FSO})}\right)\cdot\pi}} \quad (7),$$

$$w_{V\_tele}(z_{FSO}) = \sqrt{\frac{\lambda}{-Im\left(\frac{1}{q_{TV}(z_{FSO})}\right)\cdot\pi}} \quad (8).$$

Results of modelling in Figure 15 show that the beam diameter close to 150 mm (as it was defined in previous section) at the receiver side can be achieved with a beam expander with magnification M=5 ($M=f_2/-f_1$) if the distance is 200 m.

Additionally, the diameter of the laser beam on the input window of the beam expander and diameter of output window of the transmitter became clear.

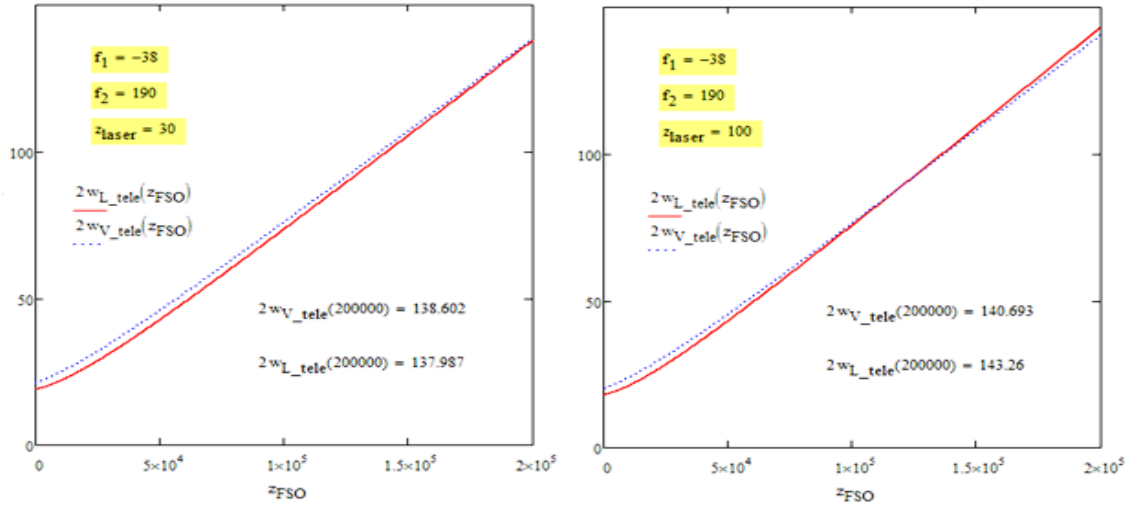

Figure 16. Graphs of the QCL laser beam spatial behavior up to 200 m distance calculated by the ABCD matrices method. Red line is displayed of lateral beam diameter, dotted -vertical (expressed in mm).

Based on the values of parameters and calculations presented above, a beam expander with adjustable 2-8 X magnification (OPBX015-003, Wavelength-Optoelectronics) was selected as the beam forming element of the transmitter.

3.2 Transmitter

The transmitter serves as a source of modulated laser beam. The beam forming and targeting elements of optical system provide detectable power density on the receiver side. The construction combined of custom design and standard opto-mechanical elements has been done using 3D graphics.

Finally, all modules were placed into the J-CH-4718-SFH (DC 12V) enclosure with IP66 environment protection that is demonstrated on Figure 17.

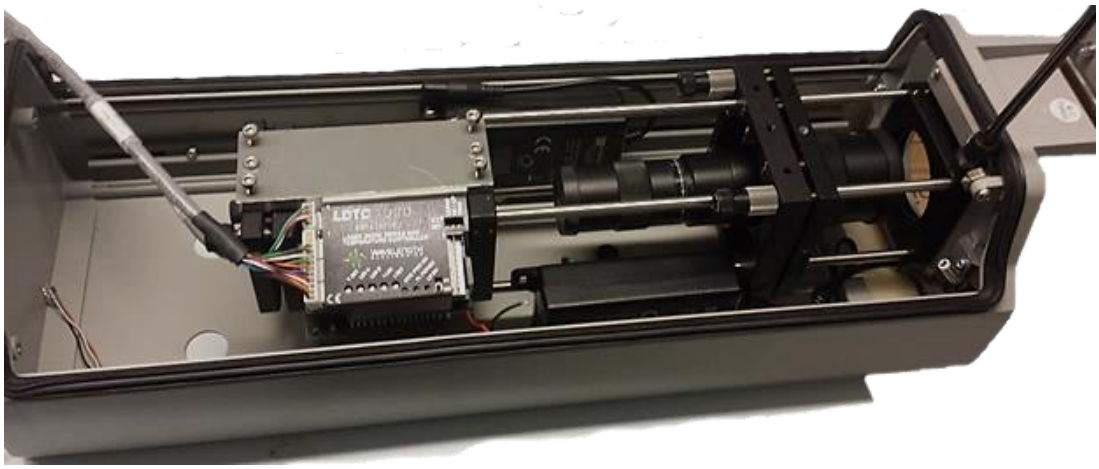

Figure 17. Displacement of the components in the transmitter housing (without thermostat module).

3.2.1 Mechanics of the Transmitter

The main element of the MIR transmitter is the QC lasers, for which is required (see Figure 18):

- Laser targeting kinematic mount,
- Beam expander adjustment mount,
- Peltier element based thermoelectric cooler (TEC),
- Cage type support frame.

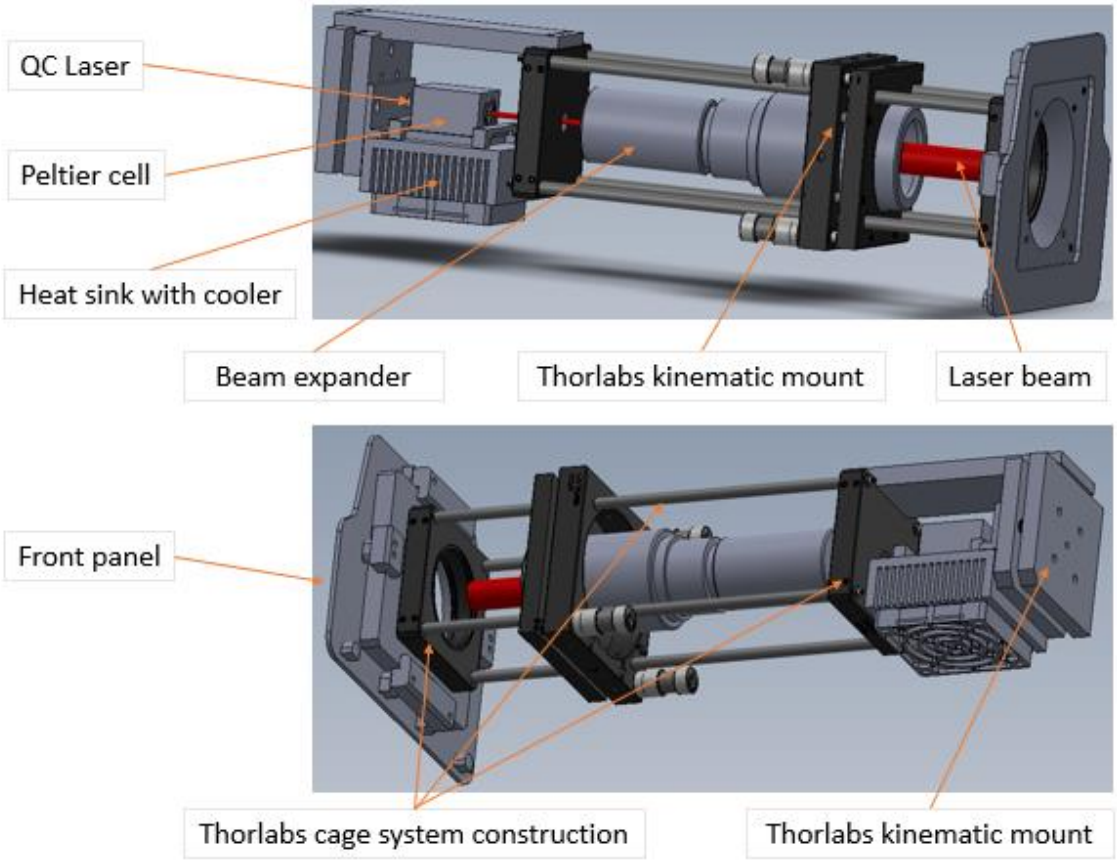

Figure 18. 3D design of the transmitter mechanics.

Rigid cage construction made of standard components keeps together all elements of the optical system and allows one to pull out of the housing the whole optical module for service work and set it back without losing of alignment. Thorlabs kinematic mounts provide precision angular adjustment of the laser and the beam expander in a milliradian scale.

3.2.2 Electronics of the Transmitter

Laser driver is responsible for the laser current, temperature, and wavelength stability. It provides adjustable laser current limits, slow-start protection of the laser diode, brownout protection, laser temperature and current monitoring.

Laser diode shutdown/interlock input is used to make pulsed operation mode of the laser with repetition rate up to 10 pulses per second and duty cycle 50%, which is feasible at integrated delayed start (time delay 100 ms). When onboard Enable switch is set to ENABLE this external

control carried out by modulator on the Arduino Nano board generating TTL-compatible pulses (Enable = Ground, Disable = Open or 3V to 5 V).

The list of electronics components of the transmitter from Figure 19 below includes:

- QC laser (AdTech)in High Heat Load package and integrated TEC (HHL13-48),
- Laser driver LDTC 1020 (Wavelength Electronics),
- Arduino Nano based modulator plate,
- Two PoE power supplies 12V and 5V, (Phihong POE21-120H, POE14-050),
- Electronic thermostat N322-NTC-2 with resistor heater and cooler (not depicted).

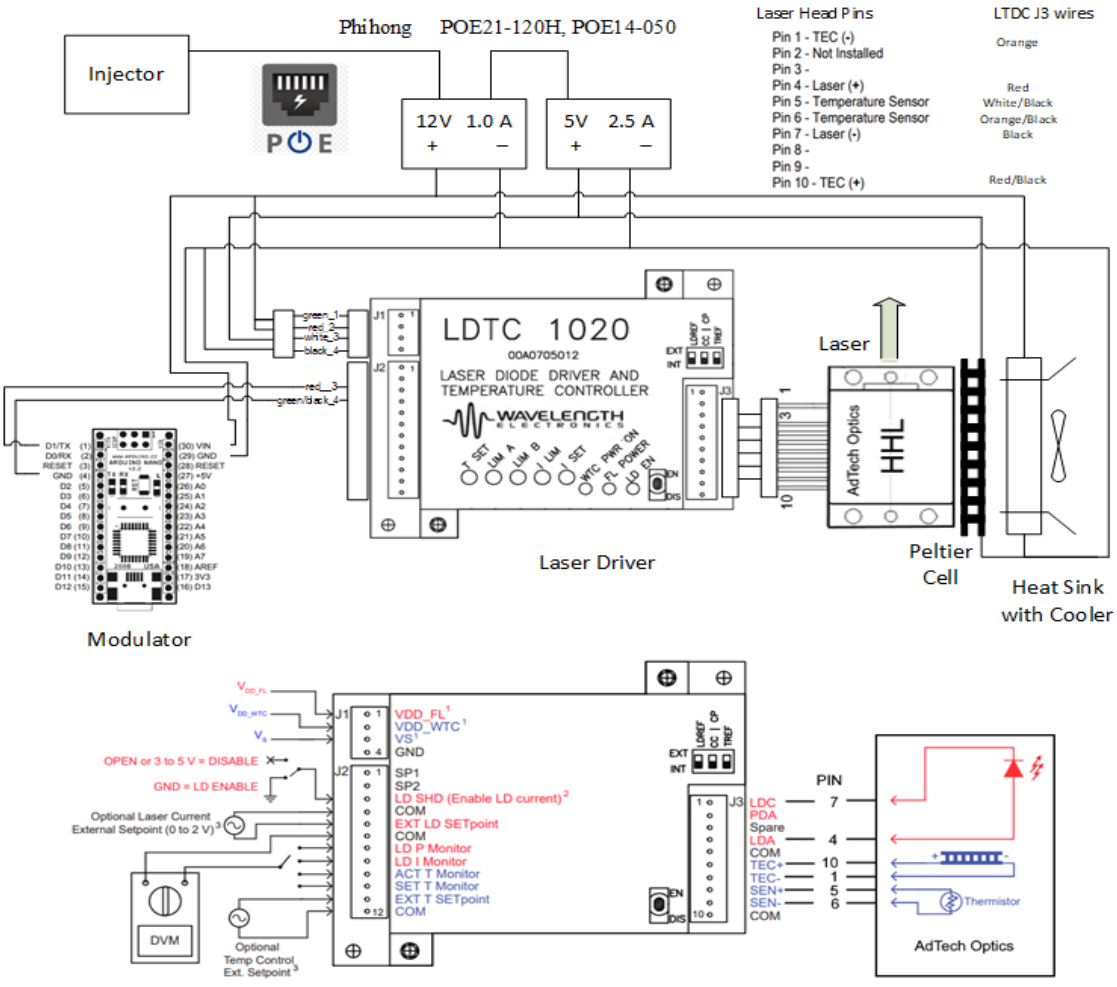

Figure 19. Electrical scheme and wiring diagram of the transmitter.

3.3 Receiver

MIR signals detection is not a simple task. If external thermal noise from radiation generated by sunlight, background radiation or objects close to the receiver is negligible due to pulsed signal, internal thermal noise of high sensitivity detectors difficult to avoid. The most suitable for outdoor use is HgCdTe (Mercury Cadmium Telluride) photodiode characterized by high absorption coefficient and quantum efficiency. Photoelectromagnetic uncooled detector based on this photodiode type with thermo-electric cooling at room temperatures was used in the receiver. At present, just a few companies produce MIR detectors with high sensitivity and high frequency bandwidth potentially suitable for FSO. Vigo System is the only company in Europe which offers complete detection system consisting of detector, pre-amplifier, cooler and power supply that fits to the requirements of the optical link prototype.

Input optics of the receiver should have a maximum available size to collect transmitted light effectively. When using a lens, its material must have high transparency in a range of wavelengths used, good mechanical strength, a resistance to all-weather conditions, non-adhesive surface. Finally, plastic Fresnel lenses were chosen as a suitable focusing optics solution.

3.3.1 Mechanics of the Receiver

Similarly to the transmitter, the receiver design has been done in 3D graphics using a combination of Thorlabs components and custom designed details. The combined mount has two-axis angular adjustment of the laser beam pointing and ability to move the laser along horizontal direction.

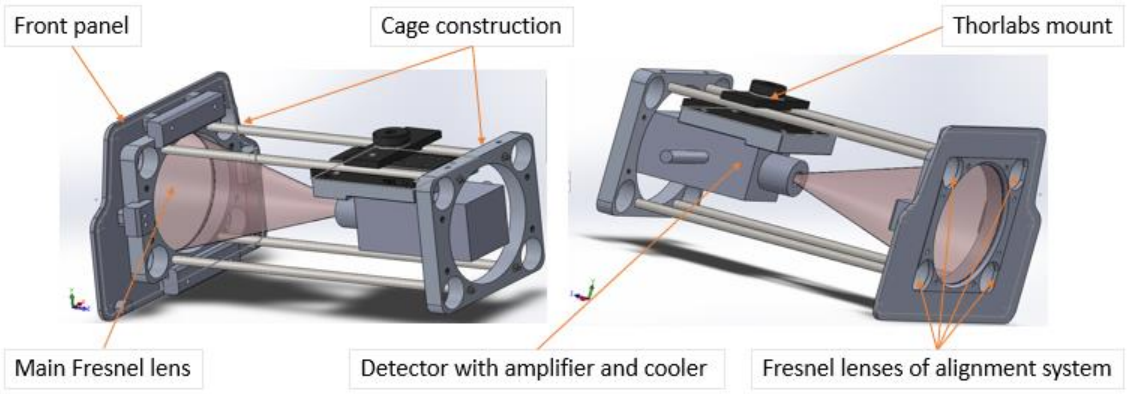

Figure 20. Receiver 3D design with parts description.

3.3.2 Electronics of the Receiver

The key component of the receiver is a photoelectromagnetic detector combined with a preamplifier from Vigo System. An exact list of electronic components used is presented below:

- PEM-10.6-1x1-T08-wBaF-48 - IR Photoelectromagnetic Uncooled Detector,
- PIP-DC-200M-F-M4 - programmable “smart” preamplifier,
- PTCC-01-BAS – standard TEC controller.

The preamplifier is accomplished by Smart Manager Software from support section of Vigo System web-page. Parameters of the pre-amplifier could be changed within factory limits and monitored as it is shown in Figure 21.

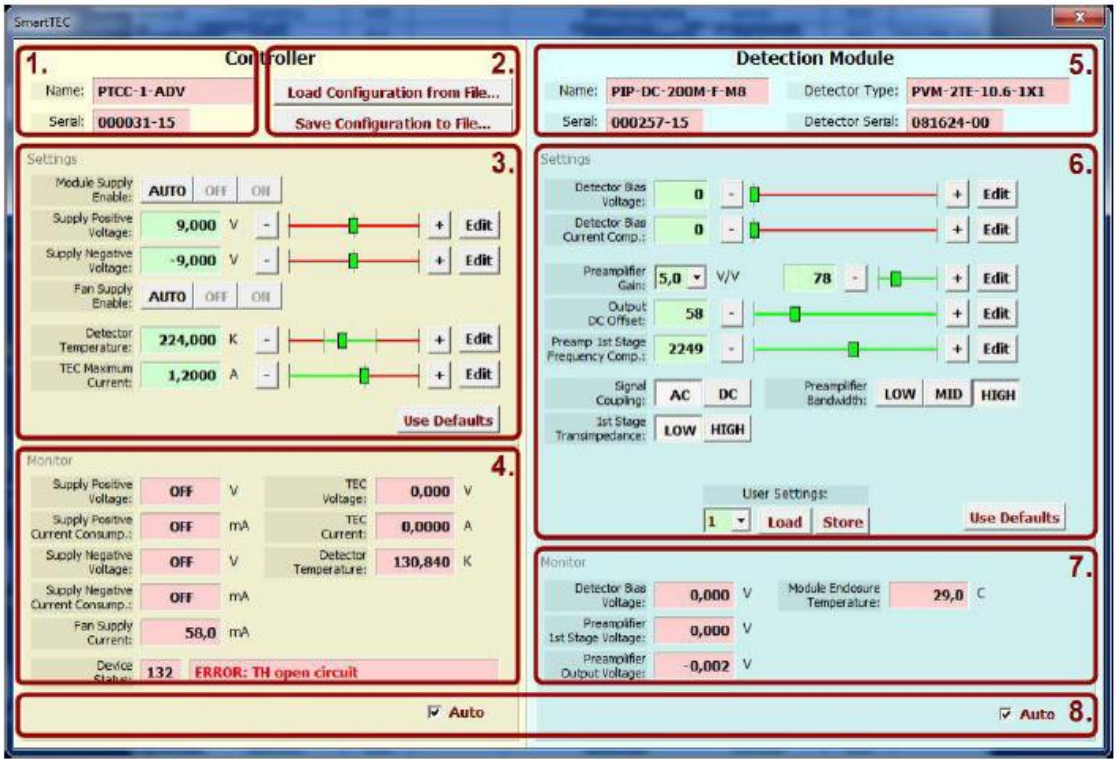

1. PTCC version & serial number
2. Storing/loading PTCC & IR detection module configuration data
3. PTCC settings
4. PTCC monitor
5. IR detection module & detector parameters
6. IR detection module settings (available only for PIP)
7. IR detection module (available only for PIP)
8. Automatic PTCC/PIP monitor update

Figure 21. Smart Manager software interface. All available parameters for adjustment are colored in green, unavailable are grayed. Picture from [21].

4 Data Acquisition System

To prove the concept of better MIR propagation through the atmospheric channel series of laboratory and on-field experiments were planned to carry out. In both cases the laser beam intensities for different wavelength must be registered with data density and time intervals suitable for further analysis. Analog signal from the receiver had to be converted to a digital signal for further processing and recording. In addition, ambient temperature, moisture as well as internal temperature of the transmitter/receiver enclosures are important to monitor at on-field all-weather tests.

4.1 IoT Technology Option

Initially it was planned to use Internet of Things technology approach (see Figure 22) to process measurements data using Arduino platform-based solutions.

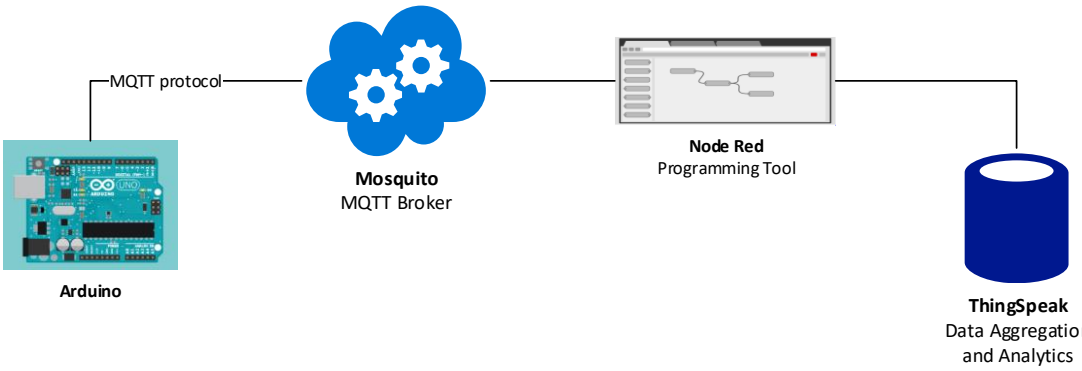

Figure 22. Simplified scheme of using of Internet of Things (IoT) technology for data acquisition.

After comparison of usage conditions offered by a row of various cloud IoT services like Microsoft Azure IoT Hub, IBM Watson IoT platform, Amazon Web Services IoT, Google Cloud Platform, Ericsson's Application Platform for IoT, and ThingSpeak the last one was found to be the most suitable for the project purposes.

ThingSpeak is an IoT analytics platform that allows us to aggregate, visualize and analyze live data streams in the cloud. ThingSpeak can be used with Arduino, Raspberry Pi, mobile and web applications to send data using Message Queuing Telemetry Transport (MQTT) protocol. The processed input data can be used to trigger a system reaction, for instance, to send a tweet when

temperature goes above a certain threshold. Attractive feature of this platform is the MATLAB support package that can be used to create MATLAB programs to process input data from controller boards.

Free usage policy: This option requires a student account with MATLAB, so that a university license can be used. Free users will be limited to sending no more than 3 million messages each year to the ThingSpeak service. For free users, the message update interval limit remains limited at 15 seconds [22].

Before use in the link prototype Arduino board and ThingSpeak connection performance was tested. The Arduino Uno based module supplied with temperature, pressure and humidity sensor BME280 was combined and programmed by Arduino open sources code for data acquisition and sending to ThingSpeak. The results of operation of the data acquisition scheme depicted in Figure 22 were recognized as negative. The most serious problem such as unstable connection with ThingSpeak server when using public channels is accompanied by the lack of sufficient time resolution for detector signal recording, low flexibility in data treatment etc. Finally, the conclusion to find a more appropriative solution has been made. This solution is described below.

4.2 Vernier Data Collection Technology

In 1996, Vernier Software & Technology company developed the first version of the Logger Pro, a general-purpose data collection and analysis computer program designed for scientific experiments. The latest version Logger Pro 3.15 is available for users with any licensed version of the software.

Luckily, a set of data collecting sensors with LabPro versatility sensor interface as well as LoggerPro software were available at the Laboratory of Automation in Metropolia University of Applied Sciences. These experiment-oriented devices became a basis the data acquisition system. By utilizing of the LabPro interface - suitable for outdoor application, supplied with user-friendly software, and capable to process data - were acquired data and arranged results of this thesis work.

4.2.1 LabPro Interface

The LabPro interface (see Figure 23) has four analog channels (CH 1, CH 2, CH 3, and CH 4) which were used for recording of analog voltage from receivers, light sensor and temperature sensors. USB computer connection was connected to laboratory notebook or a server depending on measurements type.

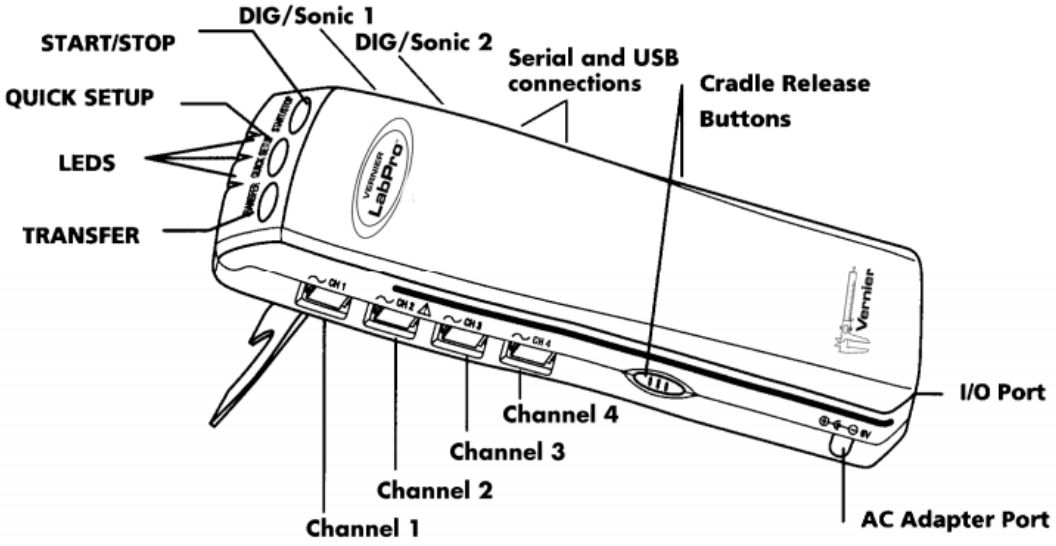

Figure 23. LabPro interface device control buttons and ports. Picture from [23]

Specifications of the LabPro interface:

- A/D conversion resolution 12bit
- Maximum sampling rate 50 000 reading per second
- Internal memory 12 000 data points
- Analog input ±10V
- Analog output ±3V, 100 mA
- Available sensors 83 types.

An attractive feature of LabPro is its ability to detect auto-ID sensors, and automatically set up an experiment. When LabPro is connected to PC via USB port Logger Pro software detects the LabPro and sensors connected [23].

4.2.2 LoggerPro Software

Logger Pro became the main program of experimental data processing in the thesis work. A wide spectrum of the software features was used in recording, calculation, modeling, and results presentation. This universal program was used even for fine adjustment of the optical link replacing an oscilloscope at maximum sample rate (see Figure 24).

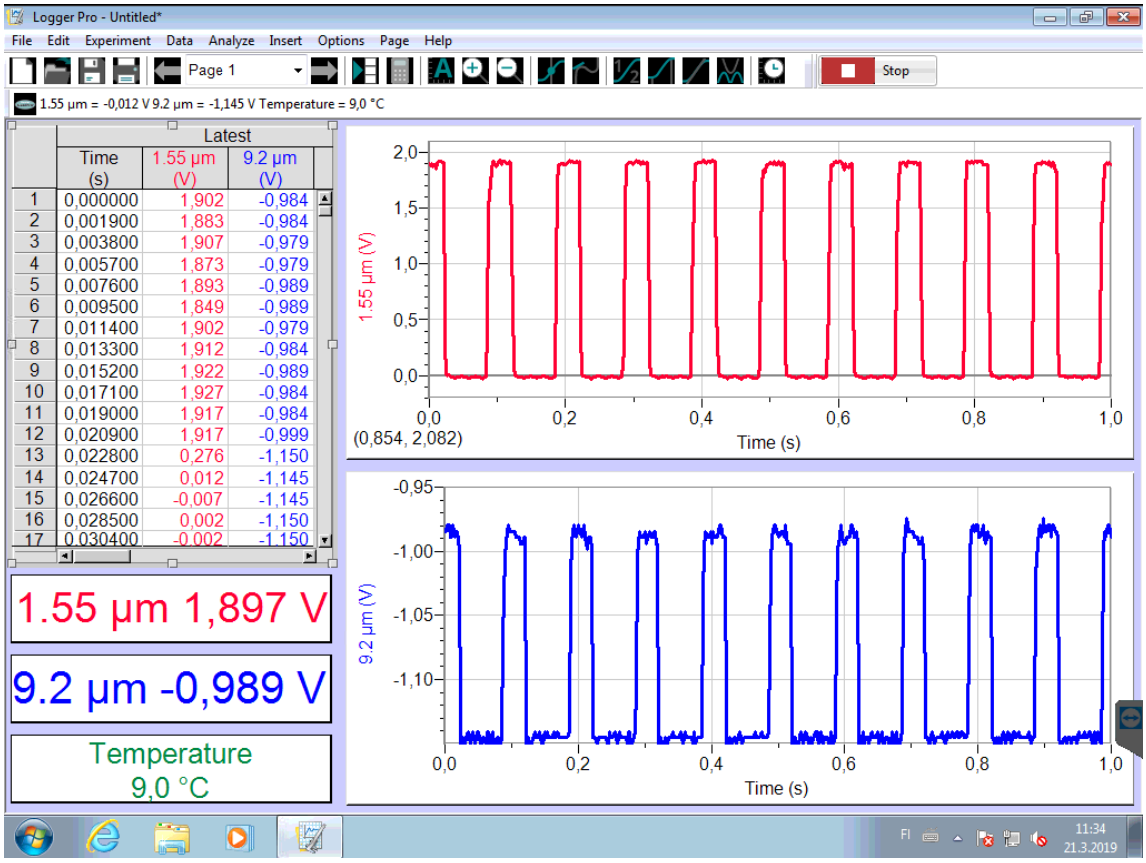

Figure 24. Oscilloscope mode of live data recording from receivers.

A description of all features of the Logger Pro can be found on the Vernier webpage [23]. The most important for our experiments were data collection functions allowing:

- Collect live data and selected events from different analog sensors,
- Manually enter data for graphing and analysis,
- Read values and slope from graphs using examine and tangent line tools,
- Lay out graphs, tables, and text across multiple pages,
- Import and export coma separated values, print graphs and data tables.

The software allows one to record long-term measurements up to 10 hours, as well as short time intervals with a high repetition rate (see Figure 25), which is well suited for measurements of fast and slow processes attenuation of an atmospheric channel.

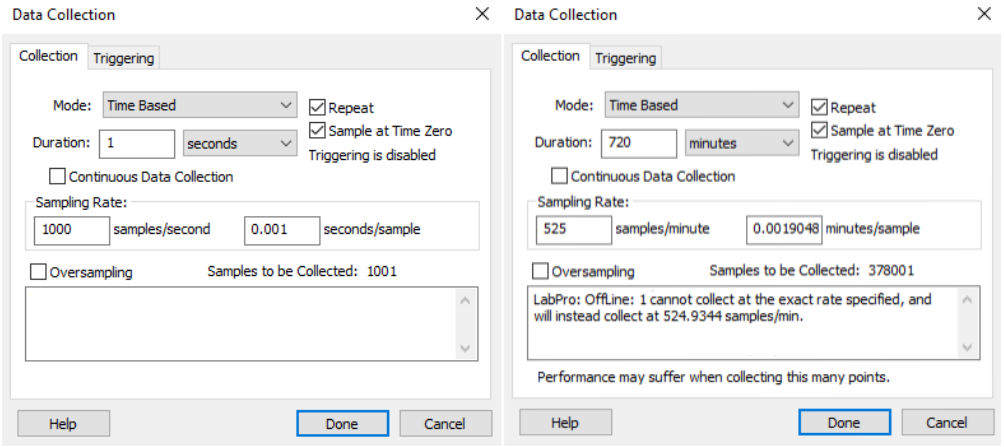

Figure 25. Examples of different recording time and sampling rate used in the experiments.

Data processing and visualization with implemented functions in Logger Pro lets to create:

- Calculated data with user-adjustable functions (see Figure 26),
- Curve fitting and close interval integral solutions
- XY graphs, double-Y graphs, and log axis graphs.

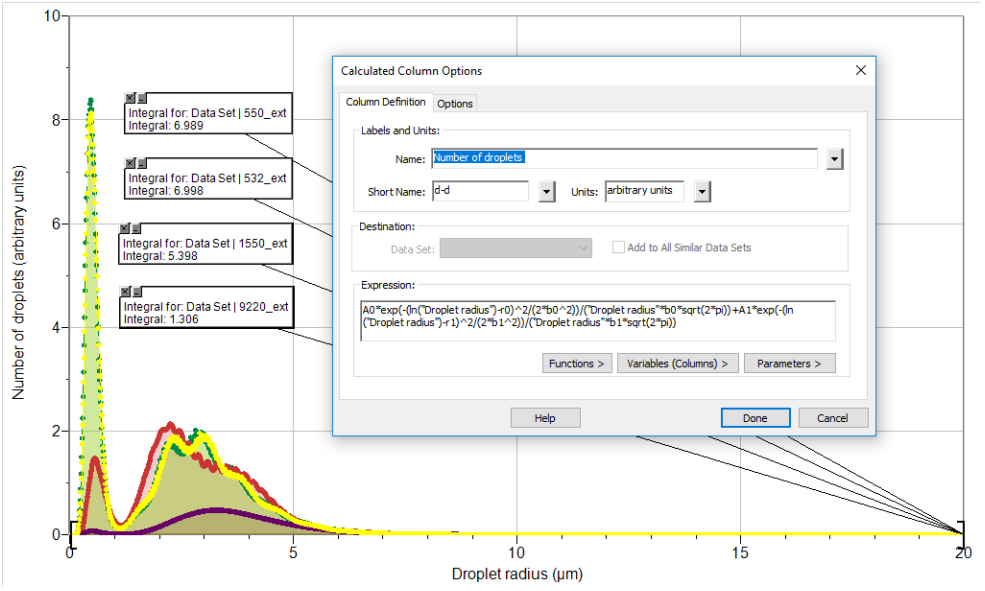

Figure 26. Artificial fog droplet size model calculation made in Logger Pro.

5 Attenuation Measurements

Interactions of light with different molecules and aerosols result in absorption and scattering of optical signals, both phenomena are wavelength-dependent. While atmospheric absorption is relatively static and simple to model, scattering loss strongly depends on the type and size distribution of the light-scattering aerosols.

As previously noted in Section 1.2 light attenuation in fogs due to Mie scattering is the strongest obstacle of FSO technology implementation. Recommendations of the International Telecommunications Union [24] for FSO link design confirm an importance of solving the problem of attenuation in fog which can reach hundreds of decibels as it shown in the International Visibility Code table presented in Appendix 2.

In theory, a scattering loss decreases with an increasing wavelength of light, but the exact level of attenuation varies with fog type. Experimental confirmation of MIR light low loss propagation by comparing attenuation NIR standard telecom diode laser light with MIR quantum cascade laser light in an ultra-sound artificial fog of different types as well as in real-life conditions was declared as one of main purposes of the project.

5.1 Laboratory Tests

As a first step, the laboratory test environment for studying of scattering properties of diverse aerosols at multiple wavelengths had been constructed. The test setup is able to emulate – in a controlled manner - different types of fog, such as advection fog and continental fog, which have different water Droplet Size Distributions (DSD) or the number of droplets of different sizes and hence attenuate different wavelengths very differently. Owing to the multi-wavelength real-time measurements, the setup makes it possible to characterize the droplet size distributions and dynamics of evolving fogs.

The setup (see Figure 27 below) consists of three optically coupled transmitters and receivers, an artificial fog chamber with a fan (see Figure 1, Appendix 3), an ultrasound humidifier with a tube of variable length, and the Vernier interface connected to a computer with the LoggerPro program.

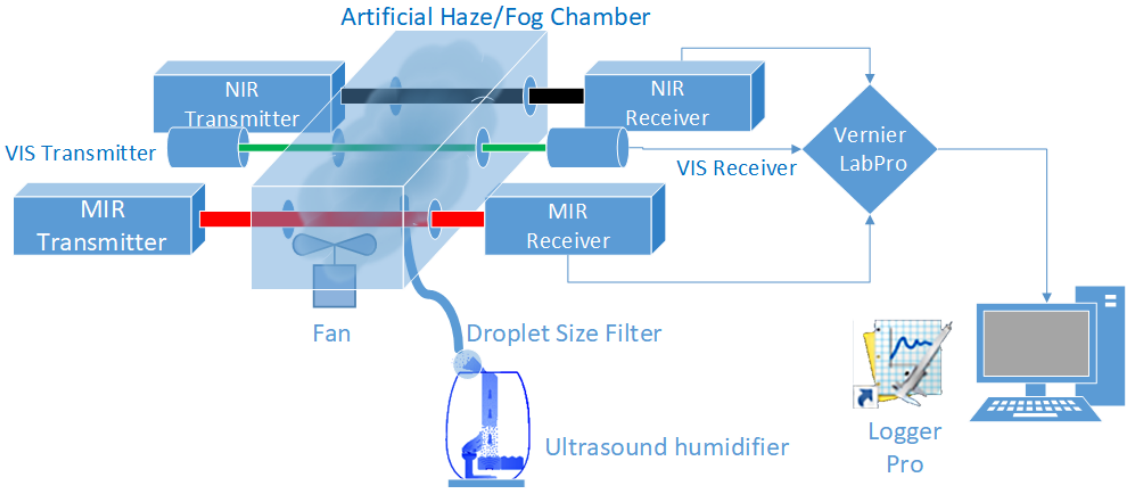

Figure 27. Laboratory test setup for light attenuation in fog research.

Measurements were carried by simultaneous recordings and comparisons of extinctions of 0.532 µm (VIS), 1.55 µm (NIR), and 9.2 µm (MIR) beams passed through homogeneously mixed artificial fog. Depending on the length of the spatial droplet filter and on additives mixed in the water, different types of fog could be generated. Tiny droplets of freshwater created continental fogs, salt water formed marine fog, and by adding ethanol and smoke were produced conditions similar to those in regions that suffer from air pollution and smog. A screenshot of intensity records made in the experiment is presented in Appendix 3 (Figure 2).

To interpret the type of fog and better understand fog evolution processes it is needed to identify its droplet composition. The following section is devoted to explanation of the droplet size distributions deduction method.

5.1.1 Droplet Size Distribution in Artificial Fog

The Beer–Lambert law determines reduced intensity of the light beam $I(\lambda, l)$ passed through the interacting media as follows:

$$I(\lambda, l) = I_0 \exp(-\beta(\lambda)\, l) \qquad (7),$$

where I_0 – initial intensity of the light beam, $\beta(\lambda)$ – extinction coefficient of interacting with the light media (comprised of absorption and scattering coefficients), λ – wavelength of the light, l – length of the media.

On the assumption that absorption and multiple scattering is negligible in the conditions of our laboratory tests, Mie theory suggests that the extinction coefficient $\beta(\lambda)$ can be deducted by summing the contributions from each water droplet size scattering by the equation:

$$\beta(\lambda)=\int_0^\infty Q(\lambda,r)n(r)2\pi r^2\,dr \qquad (8),$$

where $Q(\lambda, r)$ – scattering efficiency or scattering cross section, $n(r)$ – droplet sizes distribution, r – radius of droplet.

In order to solve the reverse task, with known extinction $\beta(\lambda)$ and efficiency $Q(\lambda, r)$ to compute distribution $n(r)$ (see Formula 8) a semiempirical approach was applied. A separately calculated set of scattering efficiencies $Q(\lambda, r)$ for selected wavelengths was transferred to LoggerPro (see Figure 28) for further theoretical extinctions coefficient calculation.

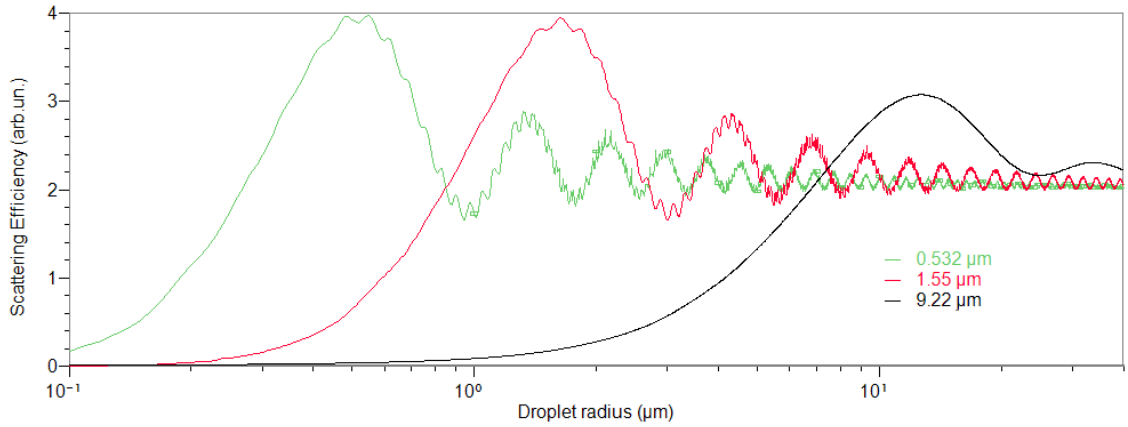

Figure 28. Real part of scattering efficiencies calculated by MiePlot software [25] for wavelengths used in the measurements.

Then, based on an accordance of experimentally measured and theoretically calculated extinction coefficients for the selected set of wavelengths DSDs were derived for various types of fogs.

The DSD is presented as a sum of probability density functions of log-normal distributions (see Formula 10 below), where μ and σ are the mean and standard deviation, and a_1 and a_2 are droplet concentration coefficients, so that

$$a_1 + a_2 = \int_0^\infty n(r)\,dr \qquad (9),$$

$$n(r) = \frac{a_1}{r}\frac{1}{\sigma_1\sqrt{2\pi}}e^{\left(\frac{-(lnr-\mu_1)^2}{2\sigma_1^2}\right)} + \frac{a_2}{r}\frac{1}{\sigma_2\sqrt{2\pi}}e^{\left(\frac{-(lnr-\mu_2)^2}{2\sigma_2^2}\right)} \quad (10).$$

Consider the above mentioned μ, σ, a, as semiempirical model parameters, by matching these parameters it is possible to obtain the *n(r)* at which the theoretically calculated extinction coefficients will be approximately equal to the corresponding coefficients from the measurements as it is show in Figure 29.

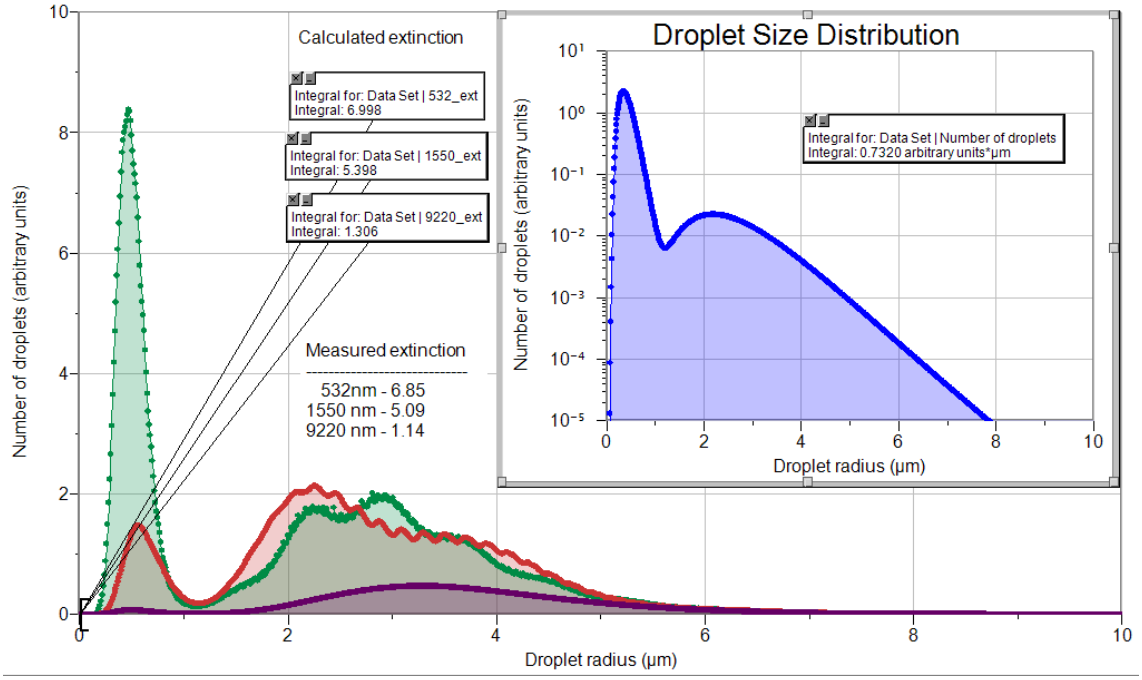

Figure 29. Screen shot of droplet size distribution calculation window of LoggerPro.

5.1.2 Visibility Estimation

It's important not only to compare attenuation of NIR and MIR laser light in our laboratory experiments, but to compare our results with those of other groups. For this purpose, the data of our measurements must be recalculated in a commonly used visibility scale.

The visibility *V* is defined as a maximum horizontal distance through the atmosphere that an object can be seen by the unaided eye. Koschmieder's law assumes a minimum contrast identifiable by an observer as 2% (0.02) at 550 nm - the maximum spectral sensitivity of the human eye under daylight conditions [26].

$$V = ln\ (0.02)/\ \beta(550) = 3.91/\ \beta(550) \quad (11).$$

Since a 550 nm light source was not used in our tests, extinction of 532 nm light *β(532)* must be transformed into extinction of *β (550)* taking in account the scattering efficiencies ratio at known droplet distribution. The value 1.044 of the transformation coefficient was obtained using the calculated extinction ratio *β(532)/β(550)* and math functions of LoggerPro. (see Figure 30). Then the Visibility axis was restored from *β(532).*

$$V = 4.08/\ \beta(532) \quad (12).$$

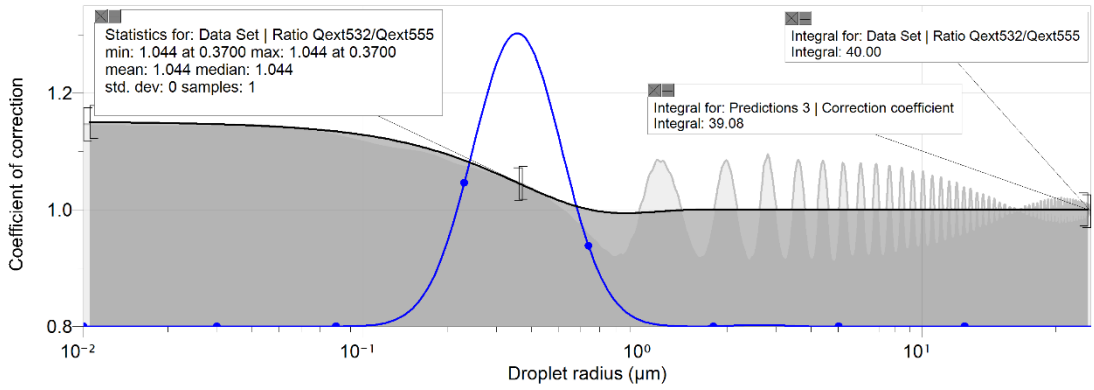

Figure 30. Correction coefficient for visibility distance calculation when using 532 nm instead of 550 nm - black, droplet distribution determined on a base of extinction ratio – blue, ratio of extinction cross-sections 532/555 nm – grey.

High density of water droplets in the artificial fog chamber makes it possible to expand calculated visibility up to hundreds of meters (see Figure 31) to compare our results with data of outdoor experiments described in [12;27]. Low level of 0.532 µm and 1.55 µm signals at high densities of the fog was compensated by extrapolation using the Curve Fit function of LoggerPro.

At the maximum concentration of water droplets in the artificial fog chamber that corresponds to about 150 m of meteorological visibility the difference in attenuation reaches 50 dB meaning that for 9220 nm transmittance is significantly better (see Figure 31).

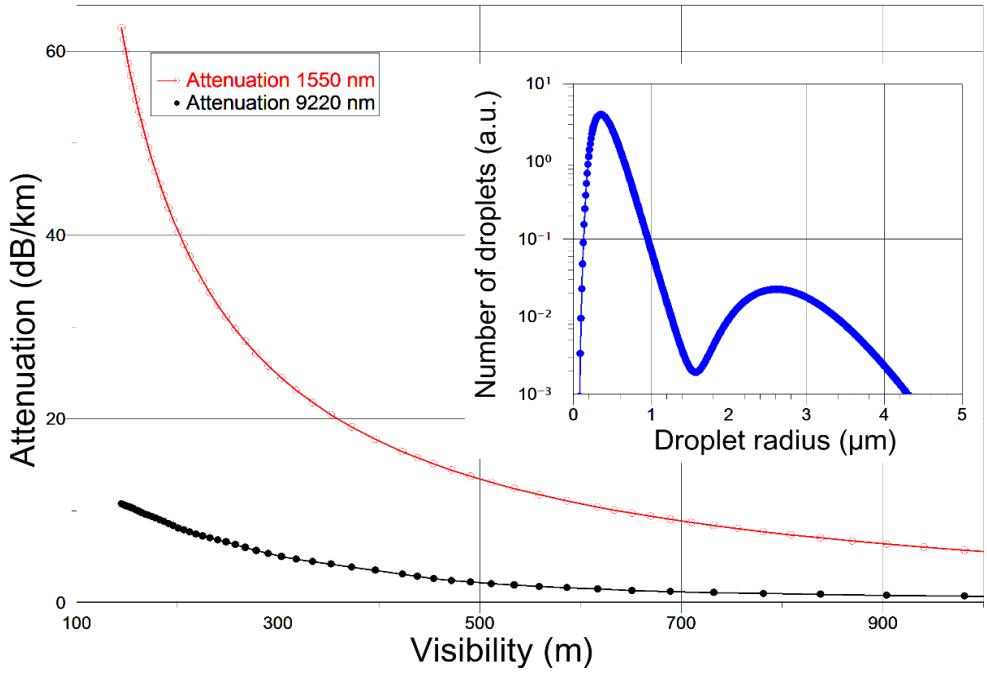

Figure 31. An example of experimentally determined attenuation of MIR and NIR laser links in fog generated in controlled laboratory conditions. DSD of inset corresponds to a visibility value of 400 m. The data is shown as a function of visibility recalculated from the 532 nm extinction.

The examples of tests with different types of fogs simulated are presented below (see Figure 32).

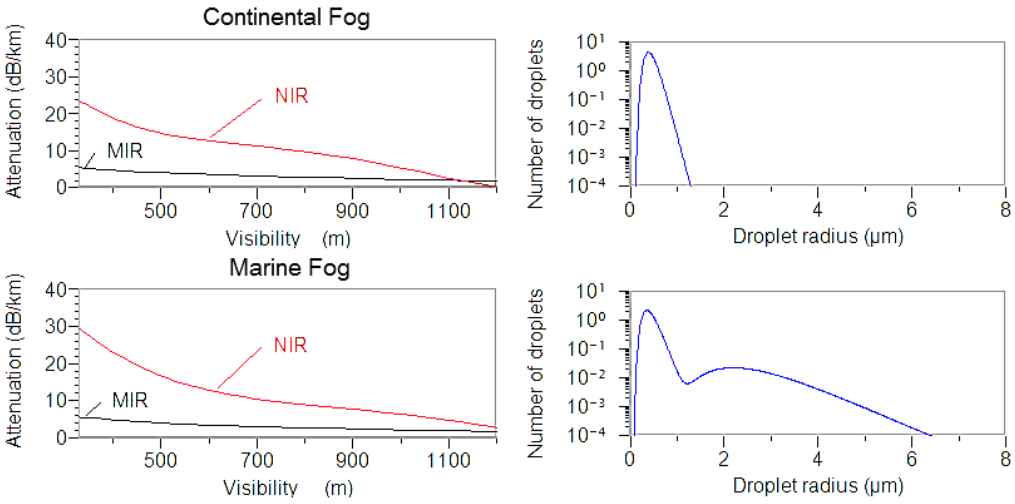

Figure 32. 1.55μm (NIR) and 9.2μm (MIR) laser beam attenuation as a function of visibility, as deduced from the controlled laboratory experiments, on the right side is DSD at the dissipation stage of the proper fog.

5.2 On-field Tests

After the laboratory tests, a targeting system of the link has been improved for long-distance outdoor measurements, and on-field experiments with high temporal resolution to study evolving fog processes have been conducted.

The photographs of the transmitter and the receiver installed on the roof of the Physicum building of University of Helsinki are demonstrated In Figure 33, the map with detailed locations of the on-field environment is attached in Appendix 4.

Figure 33. The receiver set (left) and the transmitter set (right) on the roof.

Repeating the laboratory configuration, the on-field setup environment (see Figure 34 below) consisted of the three FSO links (optically coupled transmitters and receivers). Electrical power was delivered via network cables using PoE power supplies. The analog signal of the light detectors was acquired and converted into digital by LabPro connected to a compact computer by an active USB cable. LoggerPro program software processed all data and was remotely controlled via TeamViewer [28].

The roof computer had a WiFi link to a WiFi modem router with internet access that allowed to control measurements and data transfer from any personal computer or smartphone with TeamViewer installed. Repeating mode of one second record with high (up to 1000Hz) served as oscilloscope helping in the alignment process and vibration detection. Long time and high resolution (up to 12 hours, with 525 readings per minute) records allowed to collect thorough information about fog evolution stages.

The FSO link setup was located in vicinity of the SMEAR weather station [29], so a number of meteorological parameters like ambient temperature, moisture, wind, precipitations rate, solar radiation, and visibility were available on-line as well as a database. Thereby, it was possible to

understand the behavior of optical links and reveal reasons of signal attenuation. For example, by comparing link signal fluctuations with wind speed data it became clear that the reason of signal intensity jumps was the vibration of the link mounts and roof constructions.

Long-term observations showed that dense fog is quite rare and an unpredictable phenomenon in Helsinki. So, any moment remote access to the measurements control and weather monitoring were extremely important for fog “hunting”. Finally, several fog events were recorded with good SNR and high temporal resolution to study of evolving fog processes.

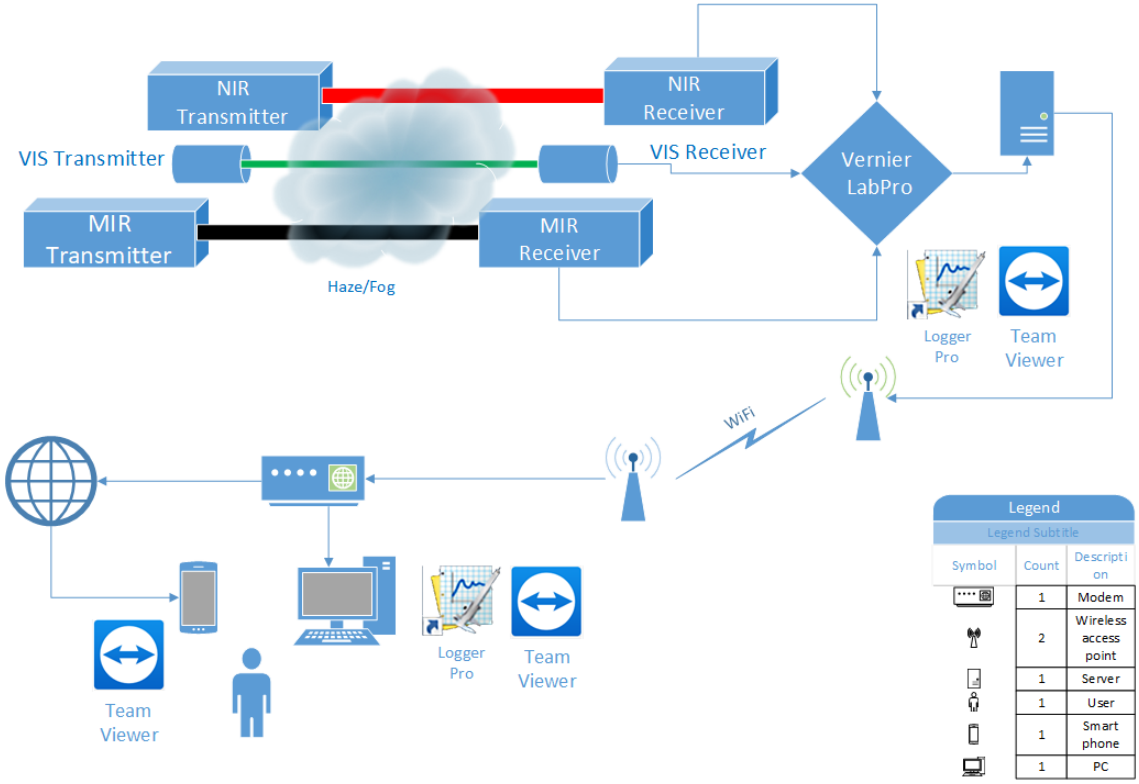

Figure 34. On-field experimental setup environment.

In the graph below (see Figure 35) there is a good example of a fog evolution from the formation to its dispersion. During the fog transformation, behavior of intensities of receiving light from NIR and MIR transmitters were very different from the visibility behavior. At a certain time interval, attenuation of NIR was stronger than of visible light and much stronger than MIR. On the other hand, fog events with stronger attenuation of MIR optical link to compare with NIR channel were recorded during the tests also.

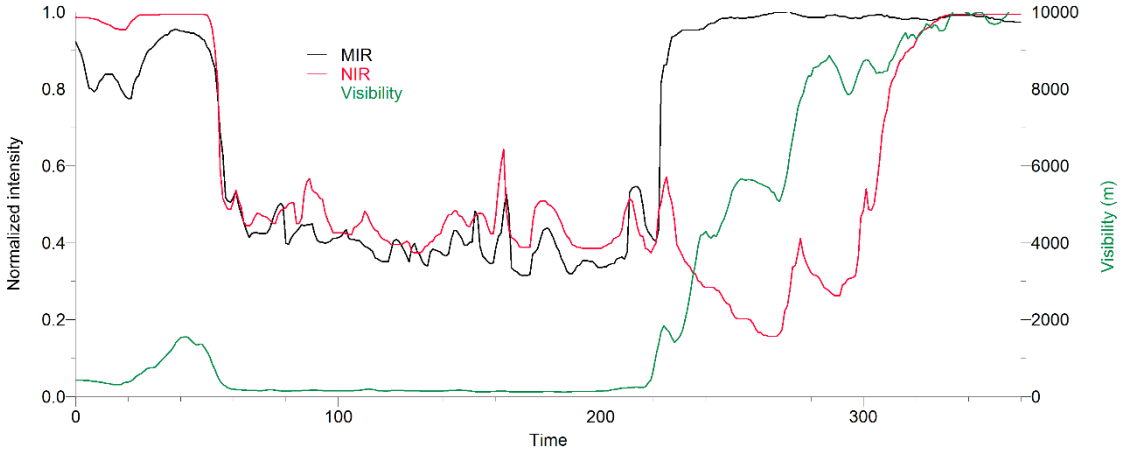

Figure 35. 1.55µm (NIR) and 9.2µm (MIR) laser beam attenuation with visibility data during a fog event on Oct 12th, 2018 in Helsinki,50 m above ground close to sea side, dense fog.

5.3 Results of the Tests

While laboratory tests of attenuation in the artificial fogs formed from water droplets with relatively narrow distribution of sizes (diameter range 1-10 µm) show clear advantage of MIR optical link, on-field tests in natural fogs with wide variation in droplet sizes (1-100 µm) show very different behavior of attenuation of visible, near-infrared, and mid-infrared laser beams.

Processes in natural evolving fog like evaporation, coagulation, precipitation occurring simultaneously at varying temperature and pressure can reproduce droplet size distributions capable attenuate any wavelength of light. The only question is how long these distributions are stable.

Unfortunately for 1.55 µm optical link, particles of radii 0.5-3 µm which cause strong attenuation for this wavelength (see Figure 28) will longer stay in atmosphere than particles of radii 8-30 µm which effectively scatter 9.2 µm. Follow the Stoke's law [30] a settling velocity of water droplet is directly proportional to the square of its radius. Hence, MIR optical link operation can be recovered upto ten times faster than NIR.

Complexity of evolving fogs conditions needs to be taken into account when designing reliable FSO links.

Unlike previously known, the near-infrared FSO link attenuation is not always correlated with visibility measurements. Especially during the fog dispersion phase, the attenuations at different optical wavelengths are difficult to estimate relying upon visibility measurements.

This is well illustrated in Figure 36, where during the same fog event (on Oct 12th, 2018) attenuation of NIR and MIR optical links is depicted on the time and visibility axes. From the bottom graph it is clearly seen that visibility data is not suitable for a 1.55 µm optical link operation forecasting.

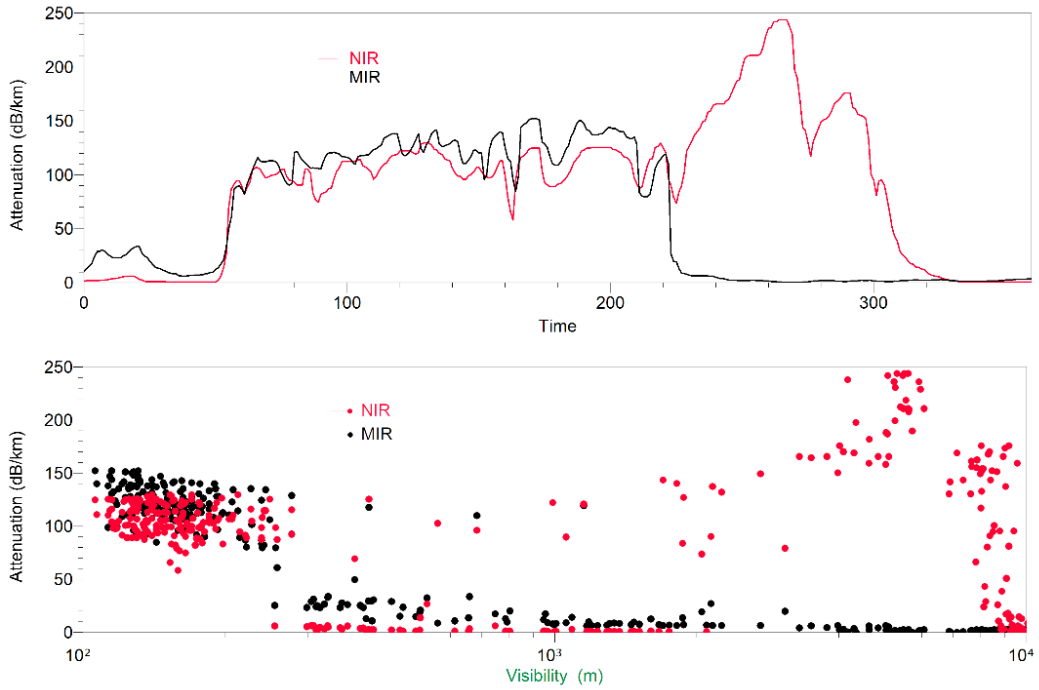

Figure 36. Attenuation of NIR and MIR optical links depending on time (upper graph) and on visibility.

6 Conclusion

The results of this thesis work confirm that the mid-infrared transmission through fog is, in most cases, better than the near-infrared transmission and middle infrared quantum cascade lasers could be considered as an effective source of signal for FSO links.

Contrary to a common assumption, our observations clearly show that near-infrared transmission of a free-space optical communication link cannot be reliably predicted based on visibility measurements.

In addition to applications in wireless optical communications, our multi-wavelength method gives information of the fog droplet size distributions and is potentially useful for measurements of fog and cloud characteristics.

One more practical consequence of our research concerns remote sensing method and device such as Light Detection and Ranging (LiDAR) that measures distance by NIR laser light. Currently, LiDARs become widely used in automotive advanced driver assistance systems, automated guided vehicles and range finding. Our results can be taken in account at design of devices for above mentioned application to avoid distance measurement errors at harsh weather condition.

References

1. "Minimum requirements related to technical performance for IMT-2020 radio interface(s)", Report ITU-R M.2410-0 (11/2017), (available at: https://www.itu.int/dms_pub/itu-r/opb/rep/R-REP-M.2410-2017-PDF-E.pdf, cited 2019-03-28)
2. M.Issa, A Wahab, "5G options and opportunities", (02/ 2016), (available at: https://www.telecomasia.net/content/5g-options-and-opportunities, cited 2019-03-28)
3. S.Hassanaly," Choosing the right connectivity for 5G", (10/2018), (available at: https://www.newtec.eu/article/article/choosing-the-right-connectivity-for-5g, cited 2019-03-29).
4. "Migrating to cloud based ran fronthaul", (available at: https://www.omnitron-systems.com/cpri-fronthaul/migrating-to-cloud-based-ran-fronthaul.php, cited 2019-03-30)
5. H. J. Son, M. M. Do "Mobile Network Architecture for 5G Era - New C-RAN Architecture and Distributed 5G Core", (10/2015), (available at: https://www.netmanias.com/en/post/blog/8153/5g-c-ran-fronthaul-kt-korea-sdn-nfv-sk-telecom/mobile-network-architecture-for-5g-era-new-c-ran-architecture-and-distributed-5g-core, cited 2019-03-31)
6. A. K. Majumdar, "Advanced Free Space Optics (FSO): A systems approach," Springer Science+Business Media, LLC, New York, (2015)
7. "Why can't we see infrared light?" (available at: https://physics.stackexchange.com/questions/209854/why-cant-we-see-infrared-light, cited 2019-03-30)
8. "Free Space Optical Communication", (available at: https://en.wikipedia.org/wiki/Free-space_optical_communication, cited 2019-03-20)
9. "Free space optic equipment", (available at http://www.ecsystem.cz/en/products/free-space-optic-equipment, cited 2019-01-18)
10. J. C. Ricklin, S.M. Hammel,F. D. Eaton, S. L. Lachinov "Atmospheric channel effects on free-space laser communication", Journal of Optical and Fiber Communications Reports, (04/2006), (available at: https://link.springer.com/content/pdf/10.1007%2Fs10297-005-0056-y.pdf, cited 2019-03-31)
11. S.Moria and Frank S. Marzano, "Microphysical characterization of free space optical link due to hydrometeor and fog effects", Applied Optics, Vol. 54, No. 22 (2015)
12. C.P. Colvero, M.C.R. Cordeiro, and J.P. von der Weid, "FSO Systems: Rain, Drizzle, Fog and Haze Attenuation at Different Optical Windows Propagation", SBMO/IEEE MTT-S International Microwave & Optoelectronics Conference, (2007), pp. 563-568
13. J.Faist, "Quantum Cascade Lasers. Dynamical Properties", Chapter 13, Published to Oxford Scholarship Online (2013), (available at http://www.oxfordscholarship.com/view/10.1093/acprof:oso/9780198528241.001.0001/acprof-9780198528241-chapter-13, cited 2019-03-31)
14. G. Chen, C. Bethea, R. Martini, P. D. Grant, R. Dudek, and H. C. Liu, "High-speed all-optical modulation of a standard quantum cascade laser by front facet illumination", Appl. Phys. Lett 95, 101104 (2009)
15. G. Chen, R. Martini, S. Park, C. G. Bethea, C. A. Chen, P. D. Grant, R. Dudek, and H. C. Liu, "Optically induced fast wavelength modulation in a quantum cascade laser", Applied Physics Letters **97** (2010)
16. C. Peng, H. Zhou, L. Zhu, T. Chen, Q. Liu, D. Wang, J. Li, Q. Peng, G. Chen, Z. Li, "Purified frequency modulation of a quantum cascade laser with an all-optical approach", Optics Letters, Vol. 42, No. 21 (2017)
17. "Gaussian Distribution. Tutorial", (available at: https://www.thorlabs.com/NewGroupPage9_PF.cfm?Guide=10&Category_ID=141&ObjectGroup_ID=16, cited 2019-03-31)

18. "Ray transfer matrix analysis", (available at: https://en.wikipedia.org/wiki/Ray_transfer_matrix_analysis, cited 2019-04-02)
19. P. A. Belanger, "Beam propagation and the ABCD ray matrices ", Optics Letters,Vol. 16, No. 4 (1991)
20. M.Scaggs "Beam Delivery: M2, BPP, Spot Size & Why You Should Care", (11/2016), (available at: https://www.laserstoday.com/2016/11/beam-delivery-m2-bpp-spot-size-why-you-should-care/, cited 2019-04-03)
21. Programmble" Smart" TEC Controller PTCC-01-ADV user's guide, (available at: https://vigo.com.pl/wp-content/uploads/2018/12/PTCC-01-ADV-user-guide.pdf, cited 2019-07-04)
22. ThingSpeak web-page, (available at: https://thingspeak.com/, cited 2019-04-02)
23. "Vernier LabPro User Manual", (available at: http://www2.vernier.com/labpro/labpro_user_manual.pdf, cited 2019-04-03)
24. "Propagation data required for the design of terrestrial free-space optical links (2007-2012), (available at https://www.itu.int/dms_pubrec/itu-r/rec/p/R-REC-P.1817-1-201202-I!!PDF-E.pdf, cited 2019-02-04)
25. P. Laven, "A computer program for scattering of light from a sphere using Mie theory & the Debye series", (available at: http://www.philiplaven.com/mieplot.htm, cited 2019-04-04)
26. "Visibility", (available at: https://en.wikipedia.org/wiki/Visibility, cited 2019-04-02)
27. P. Corrigan, R. Martini, E. Whittaker, and C. Bethea, "Quantum Cascade Lasers and the Kruse Model in Free Space Optical Communication, "Optics Express Vol.17, Issue 6, pp.5355-4359, 2009
28. TeamViewer web page, (available at: https://www.teamviewer.com, cited 2019-04-02)
29. Station of Measuring Ecosystem-Atmosphere Relation web-page, (available at: https://www.atm.helsinki.fi/SMEAR/index.php/smear-iii, cited 2019-04-05)
30. "Stoke's law", (available at: https://en.wikipedia.org/wiki/Stokes%27_law, cited 2019-04-17)
31. "Nokia Optical Anyhaul as an enabler of C-RAN", (available at: https://onestore.nokia.com/asset/192782, cited 2019-03-28)
32. T.Nguyen, "Small Cell Networks and the Evolution of 5G"(05/2017), (available at: https://www.qorvo.com/design-hub/blog/small-cell-networks-and-the-evolution-of-5g, cited 2019-04-02)

RAN Evolution and Base Station Types

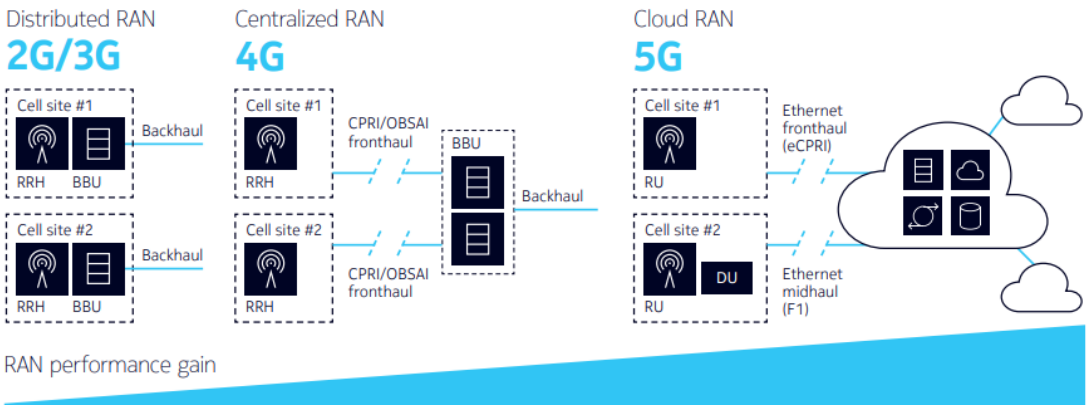

Figure 1. Radio Access Network arhitecture evolution , picture from [31].

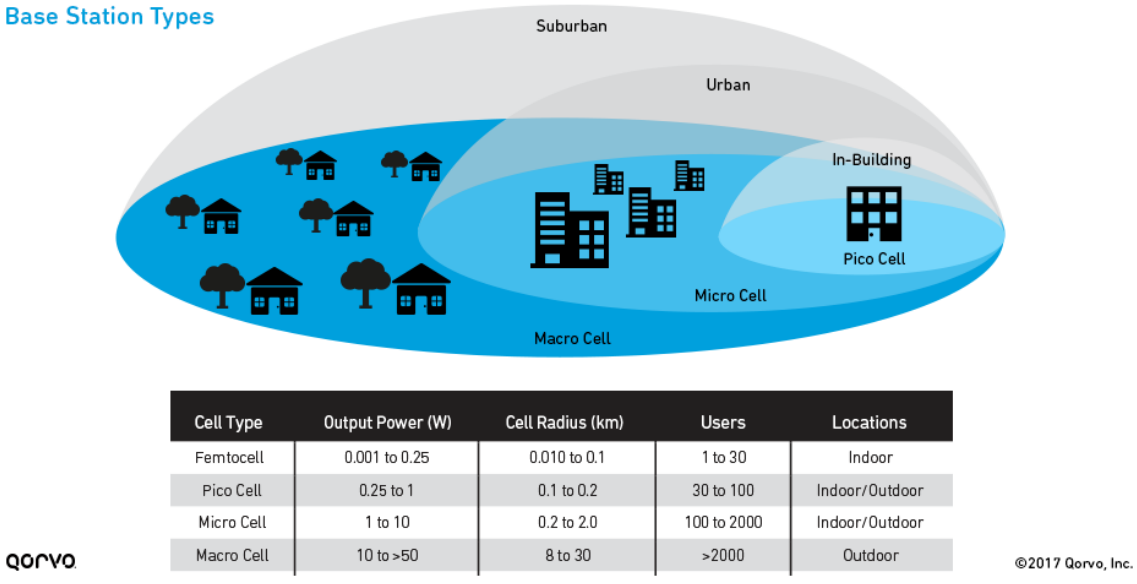

Cell Type	Output Power (W)	Cell Radius (km)	Users	Locations
Femtocell	0.001 to 0.25	0.010 to 0.1	1 to 30	Indoor
Pico Cell	0.25 to 1	0.1 to 0.2	30 to 100	Indoor/Outdoor
Micro Cell	1 to 10	0.2 to 2.0	100 to 2000	Indoor/Outdoor
Macro Cell	10 to >50	8 to 30	>2000	Outdoor

Figure 2. Mobile network small cells types, picture from [32].

International Visibility Code Table

Rec. ITU-R P.1817-1

International visibility code					
Weather conditions	Precipitation		mm/h	Visibility (m)	Attenuation (dB/km)
Dense fog				0	
				50	315
Thick fog				200	75
Moderate fog				500	28.9
Light fog		Storm	100	770	18.3
				1 000	13.8
Very light fog		Strong rain	25	1 900	6.9
	Snow			2 000	6.6
Light mist		Average rain	12.5	2 800	4.6
				4 000	3.1
Very light mist		Light rain	2.5	5 900	2
				10 000	1.1
Clear air		Drizzle	0.25	18 100	0.6
				20 000	0.54
Very clear air				23 000	0.47
				50 000	0.19

Laboratory Tests

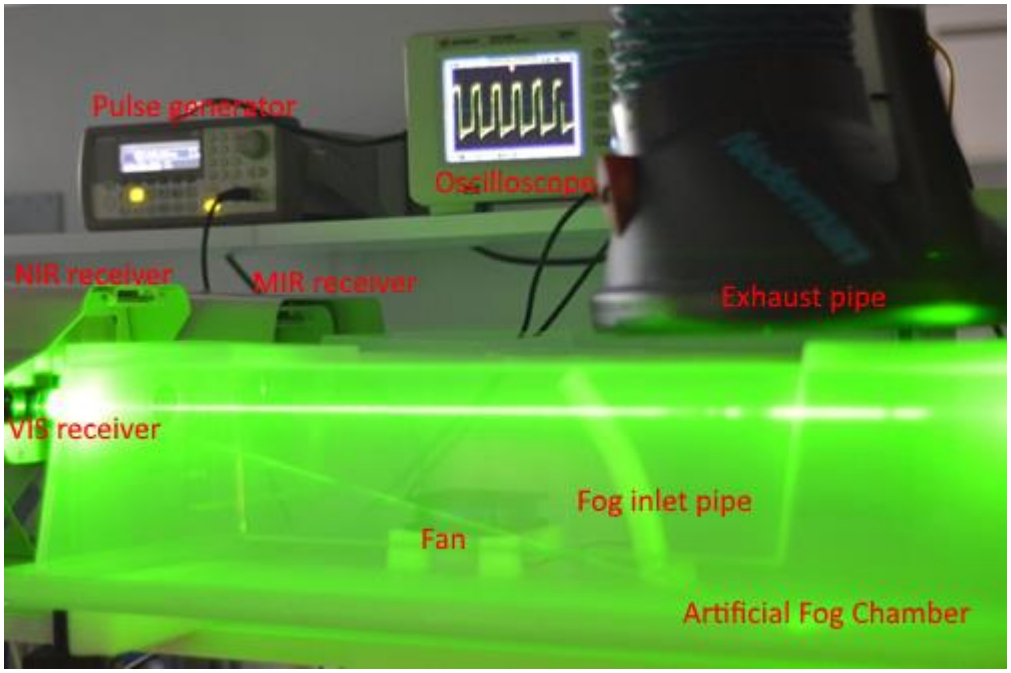

Figure 1. Photograph of the lab setup in operation.

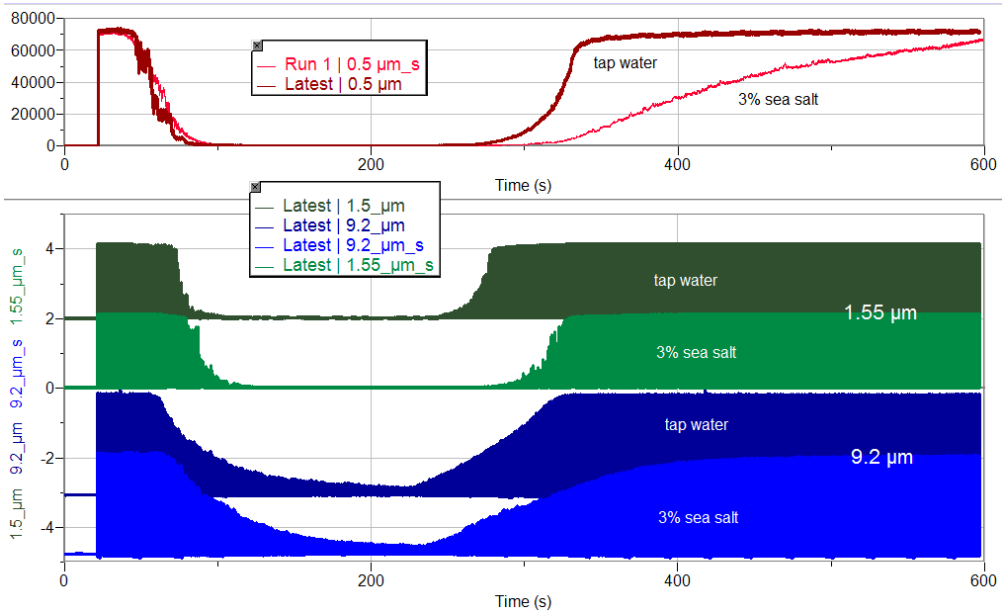

Figure 2. Screenshot of LoggerPro window with recorded intensity of the detectors signal in the lab experiments.

On-field the Optical Link Setup View

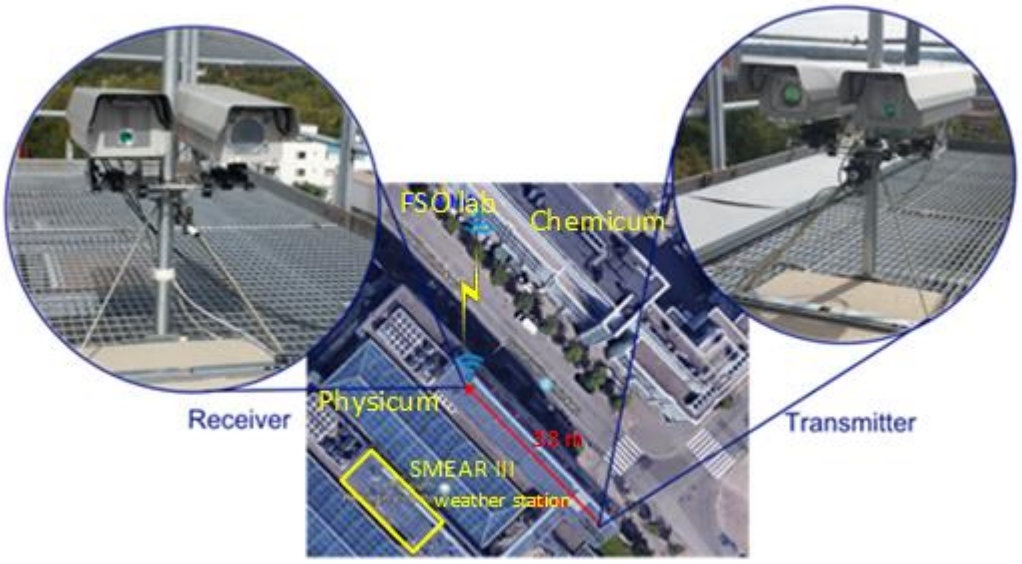

Figure 1. Satellite view of the FSO link prototype displacement.

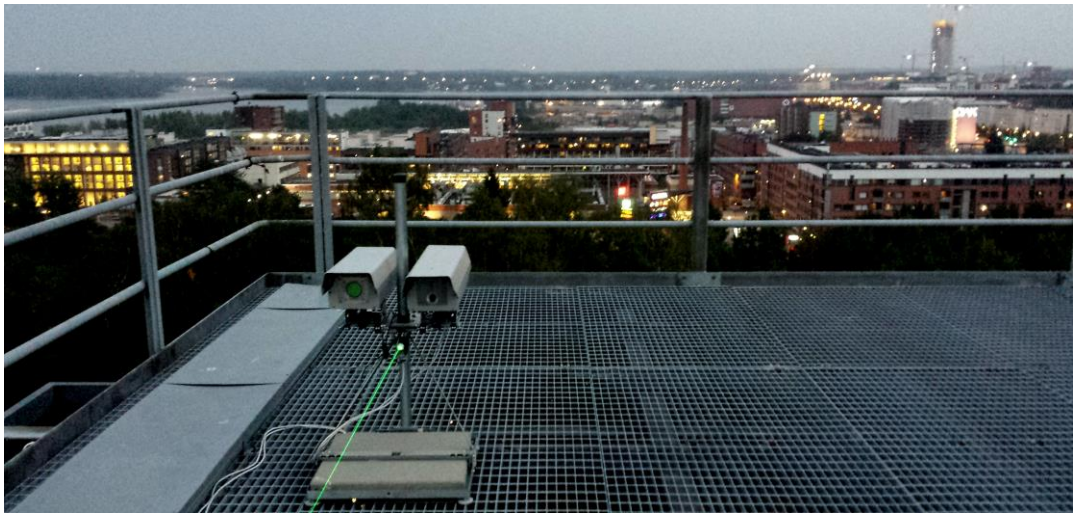

Figure 2. Late evening view of Helsinki from on-field experimental setup plate.